frontiers in Physics

TECHNOLOGY REPORT
published: 14 June 2017
doi: 10.3389/fphy.2017.00022

Myocardial T_2* Mapping with Ultrahigh Field Magnetic Resonance: Physics and Frontier Applications

*Till Huelnhagen[1], Katharina Paul[1], Min-Chi Ku[1,2], Teresa Serradas Duarte[1] and Thoralf Niendorf[1,2,3]**

[1] Berlin Ultrahigh Field Facility, Max Delbrück Center for Molecular Medicine in the Helmholtz Association, Berlin, Germany, [2] DZHK (German Centre for Cardiovascular Research), Berlin, Germany, [3] MRI.TOOLS GmbH, Berlin, Germany

Cardiovascular magnetic resonance imaging (CMR) has become an indispensable clinical tool for the assessment of morphology, function and structure of the heart muscle. By exploiting quantification of the effective transverse relaxation time (T_2*) CMR also affords myocardial tissue characterization and probing of cardiac physiology, both being in the focus of ongoing research. These developments are fueled by the move to ultrahigh magnetic field strengths, which permits enhanced sensitivity and spatial resolution that help to overcome limitations of current clinical MR systems with the goal to contribute to a better understanding of myocardial (patho)physiology *in vivo*. In this context, the aim of this report is to introduce myocardial T_2* mapping at ultrahigh magnetic fields as a promising technique to non-invasively assess myocardial (patho)physiology. For this purpose the basic principles of T_2* assessment, the biophysical mechanisms determining T_2* and (pre)clinical applications of myocardial T_2* mapping are presented. Technological challenges and solutions for T_2* sensitized CMR at ultrahigh magnetic field strengths are discussed followed by a review of acquisition techniques and post-processing approaches. Preliminary results derived from myocardial T_2* mapping in healthy subjects and cardiac patients at 7.0 T are presented. A concluding section discusses remaining questions and challenges and provides an outlook on future developments and potential clinical applications.

Keywords: magnetic resonance, MRI, ultrahigh field, magnetic susceptibility, MR technology, cardiac physiology, cardiovascular imaging, myocardial tissue characterization

OPEN ACCESS

Edited by:
Ewald Moser,
Medical University of Vienna, Austria

Reviewed by:
Bernhard Gruber,
University Medical Center Utrecht, Netherlands
Albrecht Ingo Schmid,
Medical University of Vienna, Austria

***Correspondence:**
Thoralf Niendorf
thoralf.niendorf@mdc-berlin.de

Specialty section:
This article was submitted to Biomedical Physics, a section of the journal Frontiers in Physics

Received: *24 March 2017*
Accepted: *30 May 2017*
Published: *14 June 2017*

Citation:
Huelnhagen T, Paul K, Ku M-C, Serradas Duarte T and Niendorf T (2017) Myocardial T_2 Mapping with Ultrahigh Field Magnetic Resonance: Physics and Frontier Applications. Front. Phys. 5:22. doi: 10.3389/fphy.2017.00022*

INTRODUCTION

T_2* Sensitized Cardiovascular Magnetic Resonance

Myocardial tissue characterization plays an important role in the diagnosis and treatment of cardiac diseases. Thanks to its soft tissue contrast and versatility, cardiovascular magnetic resonance imaging (CMR) has become a vital clinical tool for diagnosis and for guiding therapy of cardiac diseases [1, 2]. CMR can provide morphologic and functional information as well as insights into microstructural changes of the heart muscle [2]. Quantitative mapping of MR relaxation times which govern the MR signal evolution offers the potential of non-invasive myocardial tissue characterization without the need of exogenous contrast agents. Mapping of the effective transverse relaxation time T_2* is the subject of intense clinical interest in CMR. By exploiting the blood oxygenation level-dependent (BOLD) effect [3], T_2* sensitized CMR has been proposed as a

means of assessing myocardial tissue oxygenation and perfusion. T_2* mapping has been shown to be capable of detecting myocardial ischemia caused by coronary artery stenosis [4], to reveal myocardial perfusion deficits under pharmacological stress [5–10], to study endothelial function [11] or to assess breathing maneuver-dependent oxygenation changes in the myocardium [12–15]. Preclinical studies have also demonstrated the potential of T_2* mapping to detect structural changes in the infarcted heart muscle and even to distinguish between focal and diffuse fibrosis [16–18]. In clinical application T_2* mapping is the method of choice for quantification of myocardial iron content, an essential parameter for guiding therapy in patients with myocardial iron overload [19–23].

The linear increase of susceptibility effects with magnetic field strength together with the availability of ultrahigh field ($B_0 \geq$ 7.0 T) whole body human MR systems has fueled explorations into myocardial T_2* mapping at 7.0 T. In this context, the aim of this report is to introduce the biophysical background of T_2* as a promising MR biomarker, present challenges and technical solutions for myocardial T_2* assessment at ultrahigh magnetic field strengths, discuss its merits and current limitations, as well as to show early applications in healthy volunteers and cardiac patients along with providing a look beyond the horizon.

Biophysics of the Effective Transverse Relaxation Time T_2*

The fundamental principle behind T_2* relaxation is the loss of phase coherence of an ensemble of spins contained within a volume of interest or voxel after a radio frequency (RF) excitation. Unlike T_1 relaxation which is based on spin-lattice interactions or T_2 relaxation which is caused by spin-spin interactions both being inherent properties of tissues in a magnetic field, T_2* relaxation includes a tissue inherent part as well as contributions from external magnetic field perturbations [24]. These magnetic field inhomogeneities influence the effective transversal MR relaxation time T_2* [25, 26]. T_2* is defined as:

$$\frac{1}{T_2^*} = \frac{1}{T_2} + \frac{1}{T_2'} \tag{1}$$

with T_2 being the transverse relaxation time and T_2' representing magnetic susceptibility related contributions [27].

The most common way of T_2*-weighted imaging is gradient recalled echo (GRE) imaging. The MR signal magnitude $S_m(\theta)$ created by a spoiled GRE pulse sequence is:

$$S_m(\theta) = S_0 sin(\theta) exp\left(-TE/T_2^*\right) \frac{\left[1 - exp\left(-TR/T_1\right)\right]}{\left[1 - cos\left(\theta\right) exp\left(-TR/T_1\right)\right]} \tag{2}$$

with S_0 representing the spin density, TR the repetition time, TE the echo time defined by the time between MR signal excitation and MR signal readout [28], T_1 and T_2* are tissue specific longitudinal and effective transversal relaxation time constants and θ is the flip angle about which the magnetization is deflected by the excitation RF pulse. If TR and T_1 are being kept constant Equation (2) can be simplified to:

$$S_m(\theta) \propto exp\left(-TE/T_2^*\right) \tag{3}$$

Exploiting this relationship T_2* can be estimated by acquiring a series of images at different echo times TE followed by an exponential fit of the measured signal intensity vs. the echo time TE. This is commonly realized by using multi echo gradient echo (MEGRE) pulse sequences, which employ a series of dephasing and refocusing gradients to quickly acquire a series of T_2* sensitized images at several echo times as illustrated in **Figure 1**. T_2* weighted MRI is most sensitive to field perturbations when TE is equal to T_2* [29]. Exponential fitting of the signal decay can be done either for each voxel individually or for the mean signal within a region of interest. Single voxel fitting is more prone to noise but provides spatially resolved information in the form of relaxation maps (**Figure 1**). Besides mono-exponential fitting also multi-exponential fitting can be applied, if multiple signal compartments with different T_2* relaxation times are expected within an imaging voxel.

$$\begin{aligned} S_m(\theta) \propto\ & S_1 exp\left(-TE/{}^1T_2^*\right) + S_2 exp\left(-TE/{}^2T_2^*\right) + \ldots \\ & + S_n exp\left(-TE/{}^nT_2^*\right) \end{aligned} \tag{4}$$

Here S_1, S_2, S_n represent the relative volume fractions of the different compartments with their corresponding effective transverse relaxation times ${}^1T_2$*, ${}^2T_2$*, and ${}^nT_2$*.

T_2* relaxation is blood oxygenation level dependent and provides a functional MR contrast which serves as the basis of functional brain mapping [3, 26]. The effect results from a change of the magnetic susceptibility of hemoglobin (Hb) depending on its oxygenation state. Oxygenated hemoglobin is diamagnetic and has minor effect on magnetic field homogeneity. Deoxygenated hemoglobin in contrast is paramagnetic and causes magnetic field perturbations on a microscopic level resulting in spin dephasing and signal loss. T_2*-weighted MRI is sensitive to changes in the amount of deoxygenated Hb (deoxy Hb) per tissue volume element (voxel). T_2* changes and corresponding signal attenuation in T_2*-weighted MR images can hence result from a change in hemoglobin oxygenation or a change of the tissue blood volume fraction. The discovery of the BOLD phenomenon led to the development of functional MRI for mapping of human brain function, but also inspired research into BOLD imaging and T_2* mapping of the heart [9, 30].

T_2* sensitized imaging and mapping are widely assumed to provide a surrogate of oxygenation. Yet the factors impacting the transverse relaxation rate other than oxygenation are numerous including macroscopic magnetic field inhomogeneities, blood volume fraction and hematocrit [31]. Considering a biologic tissue with a specific blood volume fraction BVf, a hematocrit Hct, and a local blood oxygen saturation So_2, T_2* can be modeled as:

$$\begin{aligned} \frac{1}{T_2^*} = \frac{1}{T_2} + \gamma \left|\Delta B\right| = & \frac{1}{T_2} \\ & + BVf \cdot \gamma \cdot \frac{4}{3} \cdot \pi \cdot \Delta\chi_0 \cdot Hct \cdot (1 - So_2)\, B_0 + \gamma \left|\Delta B_{other}\right| \end{aligned} \tag{5}$$

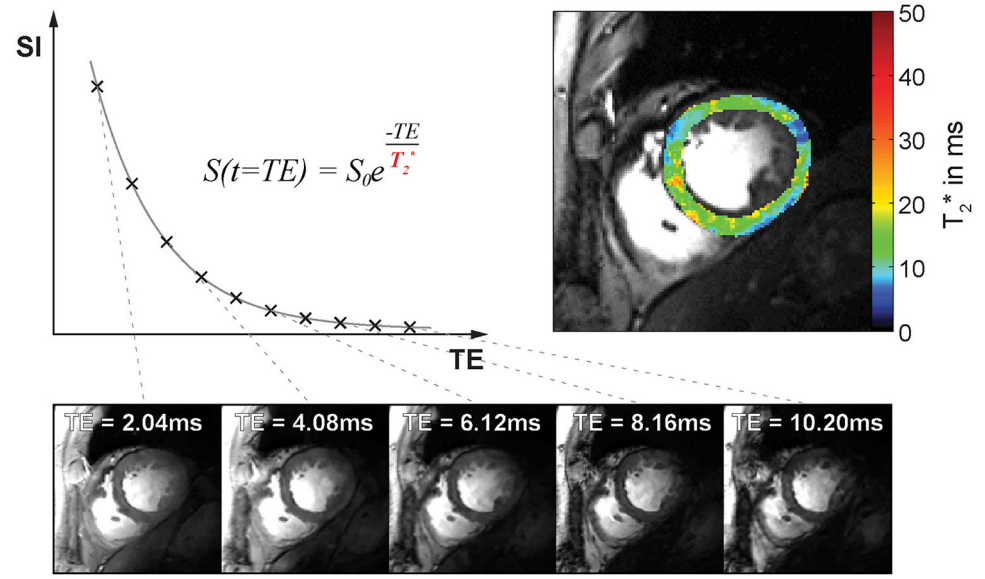

FIGURE 1 | T_2^* decay and T_2^*-weighted image contrast. Top left: Plot of signal intensity over echo time for T_2^* weighted imaging. Bottom: Example of mid-ventricular short axis views of the human heart obtained at 7.0 T. Images were acquired with increasing T_2^*-weighting (from left to right). Top right: Corresponding myocardial T_2^* map superimposed to a FLASH CINE image.

with $\gamma\,|\Delta B_{other}|$ representing additional magnetic field inhomogeneities such as macroscopic field changes [32, 33] and $\Delta\chi_0 = 3.318$ ppm being the magnetic susceptibility difference of fully oxygenated and fully deoxygenated hemoglobin (in SI units) [34]. When tissue blood volume fraction, hematocrit level and macroscopic B_0 contributions are known and echo times are greater than a characteristic time Equation (5) can be employed to non-invasively estimate tissue oxygenation using MRI [33]. It should be noted that a reduction in the tissue blood volume fraction can result in a T_2* increase which could be misinterpreted as an oxygenation increase and hence result in premature conclusions if the effect of blood volume fraction is not taken into account [35]. If all the parameters are considered correctly, T_2* can serve as a non-invasive means to probe physiology *in vivo*. It should be noted that T_2 changes, e.g., caused by alterations in tissue water content or distribution are also reflected in T_2* and hence should be considered as potential confounders.

Benefits of Myocardial T_2* Mapping at Higher Magnetic Field Strengths

The magnetization M of a material in response to an applied magnetic field is given by its magnetic susceptibility χ and the strength of the applied magnetic field H:

$$M = \chi H \tag{6}$$

This relationship results in a linear increase of magnetic field perturbations induced by microscopic susceptibility changes—the main driving force behind T_2* decay—when moving to higher magnetic fields. The effect has been confirmed for myocardial R_2* ($R_2^* = 1/T_2^*$) *in vivo* rendering T_2* mapping at ultrahigh magnetic fields ($B_0 \geq 7.0$ T) particularly appealing [36] (**Figure 2**). The enhanced susceptibility effects at 7.0 T may be useful to extend the dynamic range of the sensitivity for monitoring T_2* changes and to lower their detection level. Another advantage of performing T_2* weighted imaging and mapping at ultrahigh magnetic field strengths (UHF) is that the signal-to-noise ratio (SNR) gain achieved at higher fields can be used to improve the spatial resolution [37, 38]. This reduction in voxel sizes lowers the impact of macroscopic magnetic field gradients on intra-voxel dephasing and hence T_2* which otherwise can be a concern especially in the vicinity of strong susceptibility transitions. Transitioning to higher magnetic field strengths runs the additional benefit that the in-phase inter-echo time governed by the fat-water phase shift between the water and main fat peak of about 3.5 ppm is reduced from approximately 4.5 ms (223 Hz) at 1.5 T to 0.96 ms (1,043 Hz) at 7.0 T. This enables rapid acquisition of multiple echoes with different T_2* sensitization and facilitates high spatio-temporally resolved myocardial CINE T_2* mapping of the human heart [39]. Taking advantage of this technique, T_2* mapping at ultrahigh magnetic fields has been suggested as a means to probe myocardial physiology and to advance myocardial tissue characterization.

CHALLENGES AND TECHNICAL SOLUTIONS FOR CARDIAC MRI AT ULTRAHIGH MAGNETIC FIELDS

Enabling Radio Frequency Antenna Technology

Imaging the heart—a deep-lying target region surrounded by the lung within the large volume of the thorax—at ultrahigh magnetic field strengths poses a severe challenge due to the

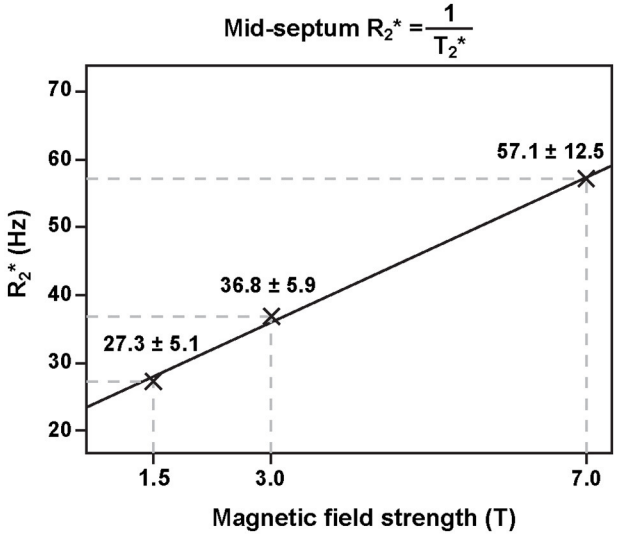

FIGURE 2 | Relation of ventricular septal R_2^* and static magnetic field strength. Myocardial R_2^* increases linearly with magnetic field strength (adapted from Meloni et al. [36] with permission from John Wiley and Sons).

short wavelength of the proton resonance frequency in tissue ($\lambda_{myocardium} \approx 12$ cm at 7.0 T). As a result, non-uniformities in the transmission field (B_1^+) can cause shading, massive signal drop-off or signal void in the images up to non-diagnostic image quality. These constraints were reported being a concern in CMR at 3.0 T [40] and were to be expected to pose a major obstacle for CMR at UHF.

A plethora of reports have evolved during the past years introducing technical innovations in RF antenna design to overcome non-uniform transmission fields. Local transceiver (TX/RX) and multi-channel transmission arrays in conjunction with multi-channel local receive arrays have been suggested as possible solutions. Eminent developments put building blocks to use consisting of stripline elements [41–45], electrical dipoles [45–51], dielectric resonant antennas [52], slot antennas [53], and loop elements [54–59]. Rigid, flexible and modular configurations have been exploited. Irrespective of the building block technology, a trend toward higher numbers of transmit and receive elements can be observed with the purpose to advance anatomic coverage [47, 54–59] and to add degrees of freedom for transmission field shaping [60].

Figure 3 compiles developments of loop element based transceiver configurations optimized for CMR at 7.0 T. A 4-channel TX/RX [55] (**Figure 3A**) and an 8-channel TX/RX [58] (**Figure 3B**) one-dimensional array were reported and extended to a 16-channel two-dimensional design [56] (**Figure 3C**). A modular 32-channel TX/RX [59] (**Figure 3D**) array further exploited the two-dimensional building block layout.

Electric dipoles hold the benefit of a linearly polarized current pattern with the RF energy being directed perpendicular to the dipole along the Poynting vector to the subject. As a consequence, the excitation field is symmetrical and uniform and comes with ample depth penetration [48] which renders electric dipoles particularly promising for MR of the upper torso and the heart. This property formed the starting point for explorations into electric dipole configurations [46–48, 50, 51]. Due to their length straight dipole elements are unfavorable if not unfeasible for high density multi-dimensional transceiver coil arrays [48]. To address this issue, the fractionated dipole concept splits the dipole's legs into segments interconnected by capacitors or inductors to achieve dipole shortening. Reduced SAR levels, moderate coupling and homogeneous B_1^+ have been reported for prostate imaging using an eight-element array consisting of fractionated dipoles [51]. A combined 16-channel loop-dipole transceiver array exploiting the fractionated dipole antenna design provided cardiac images acquired at 7.0 T exhibiting high SNR and B_1^+ transmit efficiency [50]. As an alternative, shortening of the effective antenna length can be achieved for a bow tie shaped λ/2-dipole antenna by immersing it in D_2O. Following this achievement electric dipole configurations optimized for UHF-CMR have been reported using 8 or 16 bow tie antenna building blocks [47] (**Figures 3E,F**). As a result of these research efforts, dedicated RF antenna arrays are now available which facilitate cardiac MRI at 7.0 T with rather uniform signal intensities across the heart.

In summary, explorations into enabling RF antenna technology underlined the benefits of many-channel high-density arrays for UHF-CMR.

Ancillary Devices for Cardiac Synchronization

Imaging the heart requires synchronization of the data acquisition with the cardiac cycle. Magneto hydrodynamic (MHD) effects severely disturb the electrocardiogram (ECG) [61–63] commonly applied for cardiac triggering and gating at clinical field strengths [64–66] (**Figure 4**). Distortions of the ECG's S-T segment are caused by the increased MHD impact during systolic aortic flow [67]. The S-T elevation might be mis-interpreted as an R-wave. Consequently, image quality is impaired due to the mis-detected onset of a cardiac cycle. The propensity to MHD effects is pronounced at ultrahigh magnetic field strengths [42, 68, 69]. An MR-stethoscope has been proposed as an alternative to ECG gating and triggering putting acoustic signals to use which have been reported to be immune to interferences with electromagnetic fields. With this practical solution the first heart tone of the phonocardiogram is detected, which marks the onset of the acoustic cardiac cycle. The minor latency between the onset of the electrophysiological cardiac activity and the onset of the acoustic cardiac activity allows prospectively triggered and retrospectively gated acquisitions. Acoustic triggering can hence be used with all pulse sequences that support ECG triggering without the need of sequence adjustments. Reliable trigger information has been demonstrated when using acoustic cardiac triggering and gating for UHF-CMR (**Figure 4**) [61, 68, 70]. Further alternatives for cardiac synchronization include post-processing of the ECG signal to reduce MHD induced distortions of the ECG trace [71, 72]. Wideband radar, magnetic field probes or optical systems have been proposed for physiological monitoring [73–75].

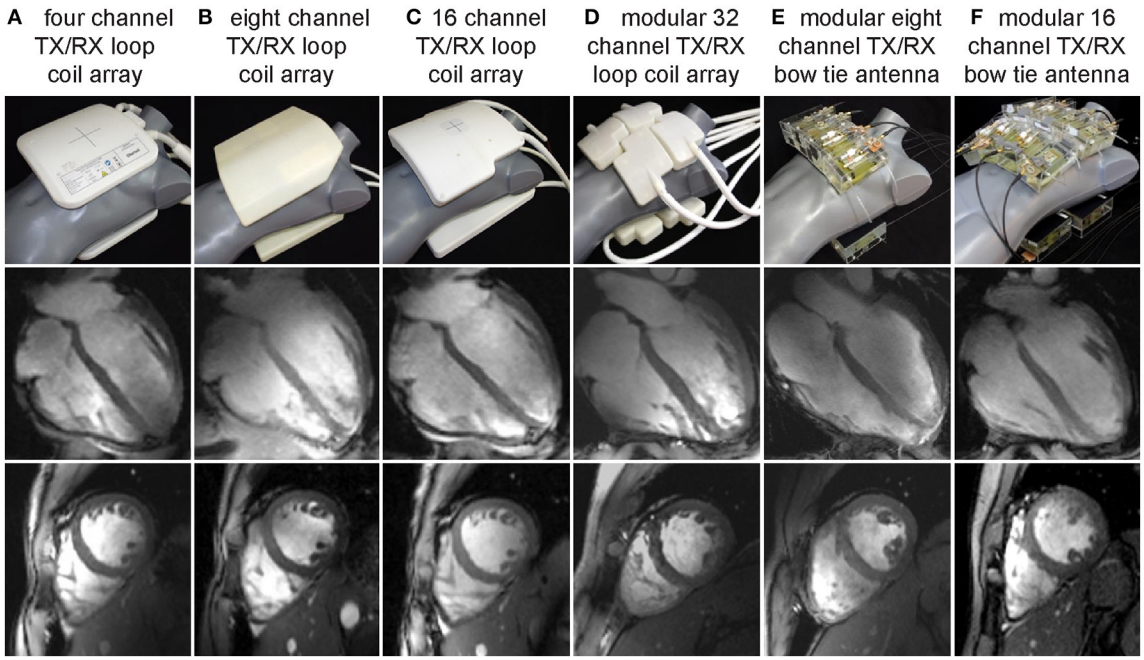

FIGURE 3 | Examples of multi-channel transceiver arrays tailored for cardiac MR at 7.0 T. Top: Photographs of cardiac optimized 7.0 T transceiver coil arrays including (left to right) **(A)** a four-channel, **(B)** an eight channel, **(C)** a 16 channel and **(D)** a 32 channel loop array configuration together with an **(E)** eight channel and **(F)** 16 channel bow tie antenna array. For all configurations the RF elements are used for transmission and reception. Center and bottom: Four chamber and short axis views of the heart derived from 2D CINE FLASH acquisitions using the RF coil arrays shown on the left and a spatial resolution of (1.4 × 1.4. × 4.0) mm^3 (from Niendorf et al. [113] with permission from John Wiley and Sons).

T_2* Imaging Techniques

T_2* sensitized imaging and mapping is commonly performed employing gradient echo imaging independent of magnetic field strength. To decrease acquisition times multi echo gradient echo techniques (MEGRE) acquiring multiple echoes after each RF excitation instead of only one echo per repetition time *TR* are recommended for fast T_2* mapping (**Figure 5A**, top). For myocardial T_2* mapping cardiac triggered segmented acquisitions are commonly performed in end-expiratory breath hold conditions to avoid respiratory and cardiac motion and to reduce related macroscopic B_0 field fluctuations.

The used echo times should be adapted to sufficiently cover the T_2* decay. As the contributing fat and water signal are oscillating at different frequencies mapping algorithms must either account for or compensate the varying signal intensity from fat and water. Acquiring T_2*-weighted images at times when fat and water are equally contributing to the MR signal (in-phase) is the simplest approach to achieve this goal. At 7.0 T this is the case for echo times being a multiple of about 0.96 ms due to the chemical shift between the main fat and water peaks of approximately 3.5 ppm (1,043 Hz). Acquisition of echoes with an inter-echo spacing of ∼1 ms constitutes a challenge due to gradient amplitude and rise time limitations, especially when large acquisition matrix sizes are used. Alternatively, interleaved acquisitions can be performed by distributing the acquisition of neighboring echoes across multiple excitations (**Figure 5A**, middle). This approach permits low inter-echo spacing even for large matrix sizes but results in longer scan times since more than one *TR* is required to acquire a full T_2* decay series. While T_2* mapping at clinical field strengths is limited to single cardiac phase acquisitions, CINE T_2* mapping covering the entire cardiac cycle is feasible at UHF [39]. This advanced capability is facilitated by two benefits of UHF-MR. First, due to transversal relaxation time shortening at ultrahigh magnetic fields, *TE* can be limited to a range of approximately $TE = 0$ ms to $TE = 15$ ms to properly sample the myocardial T_2* decay. This approach is beneficial for reducing the duration of the gradient echo trains compared to lower magnetic field strengths enabling breath held multi echo CINE acquisitions. Second, the reduced in-phase echo spacing permits acquisition of a sufficient number of echoes needed to cover the signal decay and to provide an appropriate number of data points for signal fitting. Interleaving of echo times can be combined with distributing the acquisition across multiple breath-holds to ease gradient constraints and limit breath-hold durations for each acquisition (**Figure 5A**, bottom). All described acquisition strategies are capable of producing T_2* maps of similar fidelity as illustrated in **Figure 5B** for a homogenous MR phantom resembling the relaxation properties of human myocardium. To reduce the effect of macroscopic magnetic field gradients on spin dephasing and T_2*, small voxel sizes are preferable. Of course this preference has to be balanced with SNR requirements for accurate mapping which can be challenging particularly at lower magnetic field strengths. **Figure 5B** compares the effect of slice thickness on T_2*.

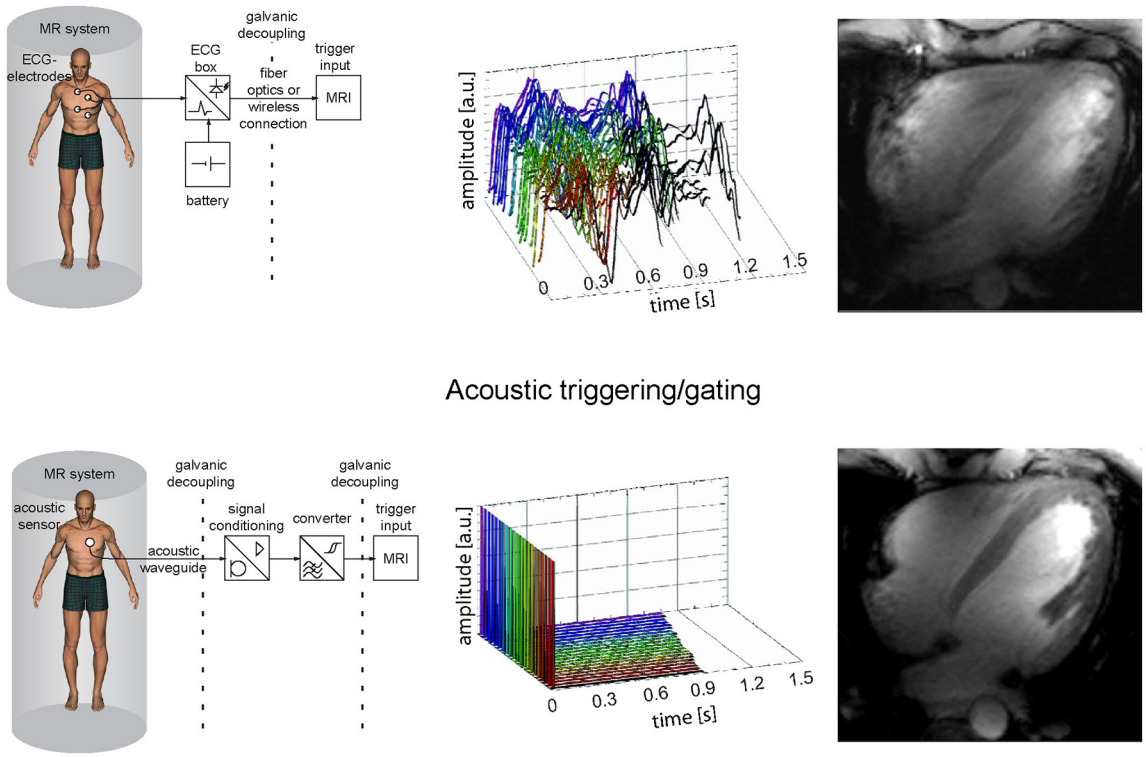

FIGURE 4 | Comparison of ECG and acoustic triggering or gating showing system schemes (left), signal traces acquired in the isocenter of a 7.0 T magnet for 18 cardiac cycles (middle) and corresponding four chamber views acquired at 7.0 T with the respective approaches (right). The ECG gated image shows severe artifacts due to incorrect cardiac synchronization, while the acoustically triggered image reveals decent image quality with good blood myocardium contrast and clear delineation of subtle structures.

While maps acquired with slice thicknesses of 6 mm or above show intra-voxel dephasing and T_2* decrease pronounced at the phantom interfaces, this effect is mitigated for slice thicknesses of 4 mm or less resulting in a more uniform T_2* map. Employing the described multi-breath hold CINE technique at 7.0 T, CINE T_2* mapping with more than 20 cardiac phases is feasible which allows monitoring of myocardial T_2* across the cardiac cycle (**Figure 6**).

In contrast to gradient echo imaging Rapid Acquisition with Relaxation Enhancement (RARE) imaging is rather insensitive to B_0 inhomogeneities, provides images free of distortion due to the use of RF refocused echoes and inherently suppresses blood signal. Cardiac RARE imaging at 7.0 T has been shown to be feasible [76]. These results—in conjunction with the challenges and opportunities of myocardial T_2* mapping at UHF—build the starting point for explorations into RARE based T_2* mapping of the heart at 7.0 T. An evolution time τ inserted after the excitation RF pulse accrues an additional phase to the magnetization that reflects the T_2* effect [77] (**Figure 7A**). As a consequence, the Carr-Purcell-Meiboom-Gill condition cannot be met and destructive interferences between odd and even echo groups configuring the signal in RARE imaging impair the image [78, 79]. Measures to account for this effect include displaced RARE [77, 80], avoiding interferences by discarding one of both echo groups, resulting in an SNR loss of factor two. Split-echo variants hold the benefit that the full available signal is maintained [81] (**Figure 7A**). A series of T_2* weighted images derived from RARE imaging using evolution times τ ranging from 2 to 14 ms is displayed in **Figure 7B** and demonstrates that the geometric integrity of the RARE images is maintained over the range of applied T_2* weighting. The corresponding T_2* map is shown in **Figure 7C**. MEGRE imaging results are shown for comparison and exhibited less myocardium to blood contrast due to the bright-blood characteristic of the technique. Consequently, the delineation of the myocardium in the corresponding T_2* map (**Figure 7C**) is more challenging compared to the RARE based T_2* map. The average effective transversal relaxation time derived from RARE imaging compares well to values previously reported for MEGRE approaches [39]. The concerns of RF power deposition and RF non-uniformity of RARE imaging were offset in this preliminary study. Split-echo RARE hence holds the potential to provide an alternative for T_2* mapping free of geometric distortion and with high blood myocardium contrast.

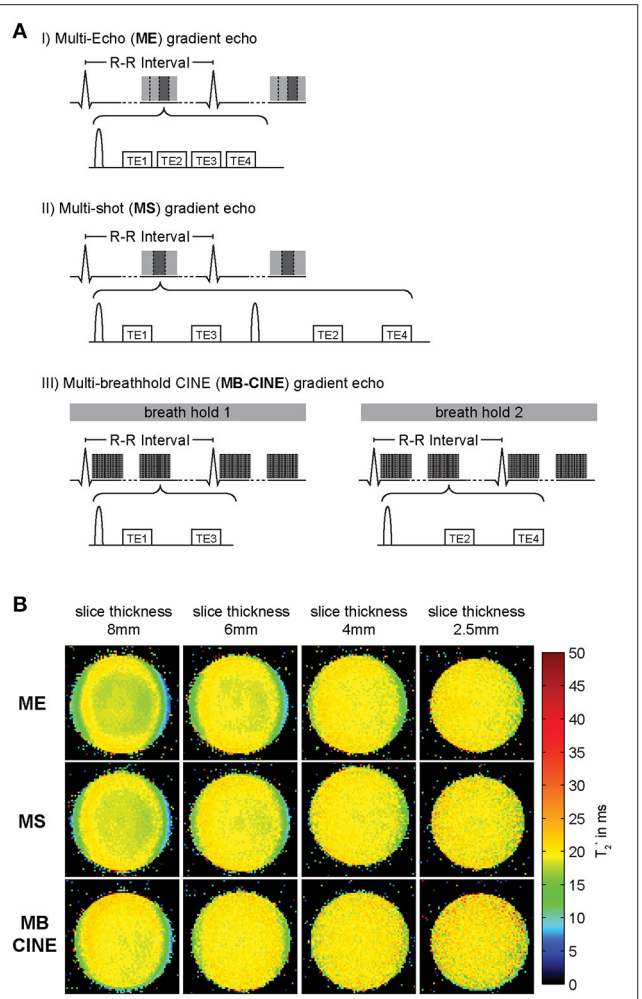

FIGURE 5 | Acquisition schemes used for T_2^* weighted imaging/mapping and corresponding T_2^* maps. **(A) (I)** multi echo gradient echo (MEGRE) acquisition, **(II)** multi shot (MS) interleaved multi gradient echo acquisition, **(III)** multi breath hold CINE (MB-CINE) interleaved multi gradient echo acquisition. **(B)** Comparison of T_2^* maps derived from a homogenous phantom resembling myocardial tissue acquired using the three different approaches and slice thicknesses from 8 to 2.5 mm. All acquisition strategies provide similar T_2^* maps. Through plane dephasing is reduced for lower slice thickness (adapted from Hezel et al. [39].)

Assessment and Control of Main Magnetic Field Homogeneity

The complex MR signal $S(r,t)$ obtained by a gradient echo technique at a location $\boldsymbol{r}$ and time t after signal excitation is given by:

$$S(r,t) = \hat{S}(t) \cdot e^{-i\phi(r,t)}, \hat{S}(t) \propto S_0 \cdot e^{-\frac{t}{T_2^*}} \tag{7}$$

$\hat{S}(t)$ is the magnitude signal, i is the imaginary unit and ϕ is the signal phase. The signal phase ϕ can be written as a function of spatial location and time [82]:

$$\phi(r,t) = \phi_0(r) - \gamma \cdot \Delta B(r) \cdot t \tag{8}$$

with γ being the gyromagnetic constant of the nucleus (for ^{1}H $\gamma = 2.675 \times 10^8$ rad/s/T) and $\Delta B(r)$ representing local magnetic field deviations with regard to the main magnetic field strength. $\phi_0(r)$ represents a constant receiver phase offset, while the time-dependent phase component $\gamma \cdot \Delta B(r) \cdot t$ is dominated by the deviation from the static magnetic field and evolves linearly over time [83]. Assuming there are no other external sources of dephasing such as, e.g., motion or flow, the signal phase ϕ serves as a direct measure of deviations from the main magnetic field B_0.

Equation (1) can be approximated as:

$$\frac{1}{T_2^*} = \frac{1}{T_2} + \frac{1}{T_2'} \cong \frac{1}{T_2} + \gamma |\Delta B| \tag{9}$$

if a linear B_0 gradient within a voxel is assumed [32]. This assumption is justified for typical voxel sizes used in cardiac T_2* mapping at 7.0 T with an in-plane spatial resolution of about 1 mm and a slice thickness of 2–4 mm [39, 84]. $|\Delta B|$ in Equation (9) includes microscopic magnetic field perturbations resulting from microstructural changes, blood oxygenation changes, iron accumulation etc. which are of diagnostic interest as well as macroscopic field changes, e.g., due to magnet imperfections or strong susceptibility transitions at air tissue interfaces. This dependency highlights the need to monitor and possibly compensate B_0 inhomogeneities when performing T_2* assessment to make sure that T_2* decay reflects microscopic susceptibility changes rather than macroscopic field perturbations.

By acquiring images at two echo times (TE), the local magnetic field variations can be calculated at each voxel by making use of Equation (8):

$$\Delta B(r) = \frac{\phi(r, TE_2) - \phi(r, TE_1)}{\gamma \ (TE_2 - TE_1)} \tag{10}$$

where $\Delta B(r)$ is given in Tesla. This procedure is referred to as B_0 mapping. It is also very common to represent local magnetic field variations in Hz by means of off-center frequency maps:

$$\Delta B_{Hz}(r) = \frac{\phi(r, TE_2) - \phi(r, TE_1)}{2\pi \ (TE_2 - TE_1)} \tag{11}$$

B_0 shimming describes the process of adjusting the main magnetic field B_0 to improve macroscopic field homogeneity. Active shimming refers to the adjustment of the main magnetic field by making use of dedicated shim coils thereby creating compensatory magnetic fields up to the 5th order of spherical harmonics [85]. Despite the existence of 5th order shim systems, most scanners provide only shim coils up to 2nd order. Active shimming options include fixed shim current settings or shimming modes based on an individual B_0 map acquired for a specific subject. For cardiac B_0 shimming a cardiac triggered field map acquisition is recommended to avoid motion artifacts. Usually a shim volume of interest is defined covering the target anatomy. Ideally the target volume should cover a small region of interest like the heart, to achieve satisfying field homogeneity

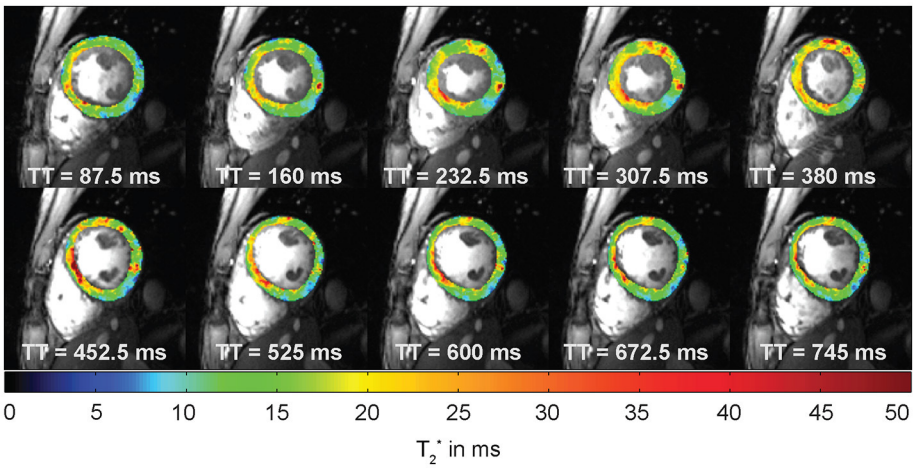

FIGURE 6 | Example of cardiac phase resolved myocardial T_2^* mapping of a short axis view of a healthy volunteer (10 out of 20 phases shown). Spatial resolution = (1.1 × 1.1 × 4.0) mm^3. Temporal resolution = 37 ms. T_2^* variations can be observed across the cardiac cycle. TT indicates the time since the trigger.

even when a limited order of shim coils is available. **Figure 8** compares B_0 homogeneity in the heart of a healthy subject at 7.0 T after applying a volume shim (**Figure 8A**, top), which is focused only on the heart and after applying a global shim (**Figure 8A**, bottom) which includes the entire field of view. Volume selective shimming was found to lead to a significant improvement in macroscopic B_0 homogeneity vs. global B_0 shimming (**Figure 8B**) [39].

Due to increased susceptibility effects, magnetic field inhomogeneities are pronounced at higher magnetic field strengths [36] (compare Equation 6). This is often a concern for T_2* weighted imaging or T_2* mapping at high and ultrahigh magnetic fields. However, by employing dedicated shimming approaches, a mean peak-to-peak off-resonance frequency across the human heart of 80 Hz [39] was reported at 7.0 T. For the left ventricle a B_0 peak-to-peak difference of approximately 65 Hz was observed at 7.0 T after volume selective shimming [39]. These results were obtained with a second order shim system so that the same level of B_0 uniformity reported here should be achievable with the current and next generation of 7.0 T scanners. The frequency shift across the heart obtained at 7.0 T compares well with previous 3.0 T studies which reported a peak-to-peak off-resonance variation of (176 ± 30) Hz over the left ventricle and (121 ± 31) Hz over the right ventricle with the use of localized linear and second-order shimming [86]. The use of an enhanced locally optimized shim algorithm, which is tailored to the geometry of the heart, afforded a reduction of the peak-to-peak frequency variation over the heart from 235 to 86 Hz at 3.0 T [87]. Another study showed a peak-to-peak off-resonance of (71 ± 14) Hz for short axis views acquired at 1.5 T [88] using global shimming. While dedicated shim routines revealed competitive results at 7.0 T vs. lower magnetic fields strength, the feasibility of using these approaches in a clinical setting remains to be investigated.

The achievement of macroscopic B_0 homogeneity across the heart at 7.0 T which is competitive with that obtained at lower magnetic field strengths provides encouragement to pursue susceptibility-based myocardial T_2* mapping at ultrahigh fields. Yet, with the arrival of CINE T_2* mapping techniques enabled by 7.0 T [39], also temporal B_0 fluctuations across the cardiac cycle and their implications on T_2* need to be considered for a meaningful interpretation of dynamic T_2*-weighted acquisitions. Temporal B_0 variation across the cardiac cycle was reported to be negligible at 1.5 T [89], but due to the increase of susceptibility effects at ultrahigh fields further investigations of this potential confounder were required at 7.0 T. It should be noted that T_2*-weighted contrast is determined by magnetic field gradients rather than absolute magnetic field strength, thus it is essential to investigate the change of these gradients over the cardiac cycle. This was done at 7.0 T by assessing macroscopic B_0 gradients across the cardiac cycle in the heart of healthy volunteers together with high temporal and spatial resolution T_2* maps [84, 90]. T_2*-weighted series of short-axis views were acquired using a MEGRE CINE approach (**Figure 9A**, top) for cardiac phase resolved B_0 and T_2* mapping. Temporally-resolved B_0 maps of the heart were calculated (**Figure 9A**, middle). Macroscopic intra-voxel field gradients were determined for each cardiac phase and their fluctuations were analyzed across the cardiac cycle. The septal in-plane gradients were found to be significantly larger compared to through-plane gradients within a voxel [with a mean in-plane field dispersion of (2.5 ± 0.2) Hz/mm against the a mean through-plane field dispersion of (0.4 ± 0.1) Hz/mm] [91].

In order to evaluate how these B_0 gradients affect T_2* measurements, the B_0 gradient-induced change of T_2* represented as ΔT_2* was estimated [84, 91]. **Figure 9B** shows the plot of mean septal T_2*, intra-voxel B_0 gradients and estimated gradient-induced ΔT_2* over the cardiac cycle averaged over a group of healthy subjects. The mean septal T_2* per cardiac phase was found to vary over the cardiac cycle in a range of approximately 23% of the total mean T_2* for all phases. Yet, the temporal range of mean ΔT_2* induced by the calculated intra-voxel macroscopic B_0 gradients represented

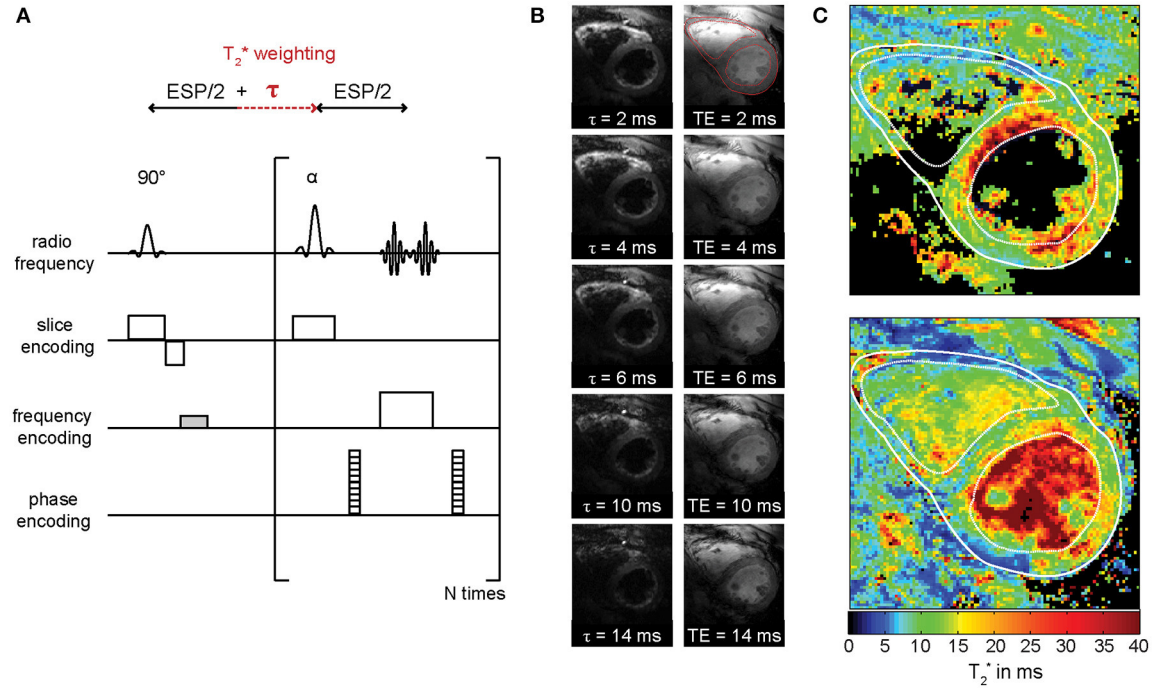

FIGURE 7 | RARE-based myocardial T_2^* mapping at 7.0 T. **(A)** Basic pulse sequence diagram of T_2^* weighted split-echo RARE. T_2^* weighting is introduced into RARE by adding an evolution time τ after the excitation RF pulse. The dephasing gradient in frequency encoding direction is imbalanced (marked in gray) to avoid destructive interferences between odd and even echo groups. **(B)** T_2^*-weighted split-echo RARE images of a short axis view employing evolution times ranging from τ = 2 ms to τ = 14 ms (left). MEGRE images obtained with echo times ranging from 2 to 14 ms (right). For improved visualization, the images do not exhibit identical windowing over the range of increasing susceptibility weighting. The myocardium was delineated and the contour is shown in the images with minimal τ/TE. **(C)** T_2^* maps derived from data in shown in **(B)** are depicted for the RARE (top) and the GRE (bottom) approach. The contours defined in the images with minimal τ/TE were copied to the T_2^* maps for better delineation of the myocardium.

only a 5% change of total mean T_2*. The remaining 18% were suggested to reflect microscopic B_0 gradient changes (potentially caused by physiological events) rather than macroscopic field inhomogeneities [84, 91].

In summary it can be concluded that if careful shimming is applied, macroscopic magnetic field inhomogeneities are not of concern for myocardial T_2* mapping even at a magnetic field strength as high as 7.0 T. Also dynamic B_0 fluctuations across the cardiac cycle can be considered negligible in the ventricular septum. These findings represent an essential prerequisite for meaningful interpretation of myocardial T_2* and its dynamics across the cardiac cycle.

Data Post-processing

The effective transverse relaxation time T_2* can be estimated by fitting an exponential function to a series of gradient echo images with different T_2* weighting, i.e., different echo times (compare Equations 3, 4; **Figure 1**). A common way of calculating such a fit by avoiding non-linear fitting procedures, is to calculate the natural logarithm of the acquired signal intensities and apply a least squares linear fit to the resulting data. This procedure is fast and produces the best solution to represent the linearized data in a least squares sense. Further to this, non-linear fitting approaches which can be applied directly to the measured data are available. The algorithms employ non-linear models in conjunction with optimization algorithms like Levenberg-Marquardt or Simplex [92]. Iterative non-linear fitting algorithms can provide improved fitting accuracy, but can be prone to careful initialization. Fast linear fitting can be used to initialize non-linear fitting algorithms leading to increased robustness and faster convergence. Irrespective of the kind of employed fitting procedure, care should be taken for voxels with intensities being at the noise level and hence potentially deteriorating the fit quality. Low SNR is a common problem particularly for myocardial T_2* mapping where acquisition times are often limited by the tolerable breath hold time. Such voxels should either be excluded from fitting—a procedure referred to as truncation—or included in the fit model as a constant noise term.

Most commercial MR systems support exponential fitting algorithms as part of the systems' software, but using customized fitting routines is often beneficial for research. First, it is often unclear what model or fitting approach is used by commercial software and how good the fit quality was, i.e., how well the fit describes the measured data. Measures like the coefficient of determination R^2 or the standard deviation of the T_2* fit [93] should be used to evaluate the reliability of the results. Taking fitting results for granted without considering fit quality

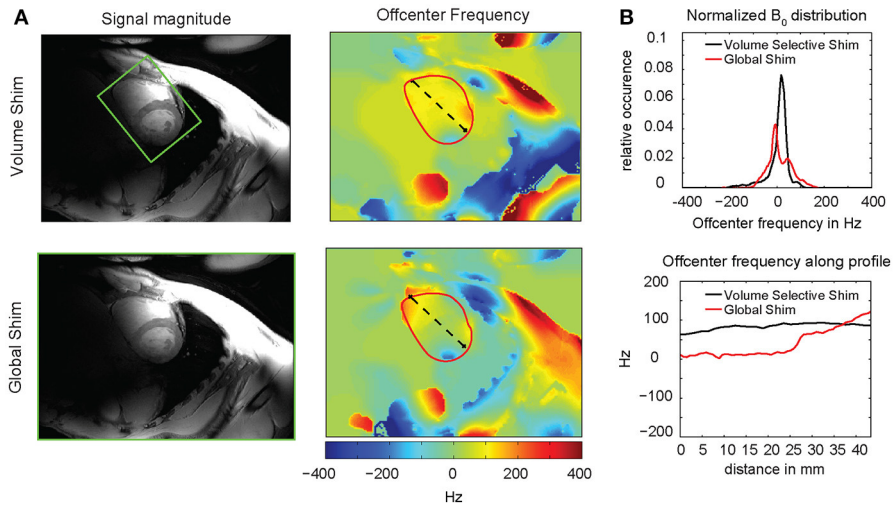

FIGURE 8 | Comparison between volume and global B_0 shimming in the heart of a healthy volunteer at 7.0 T. **(A)** left: placement of the adjustment volume in a magnitude image. **(A)** right: B_0 maps with the region of interest (red) and a profile across the heart through the ventricular septum (dashed black line) overlaid. **(B)** Plot of the histogram detailing the distribution of B_0 in the ROI outlined in the B_0 maps (top) and plots along the profile in the B_0 map (bottom) of volume selective (black) and global (red) shim. A clear improvement of field inhomogeneity can be observed after volume selective shimming indicated by a narrowing of the histogram and a flattened B_0 profile.

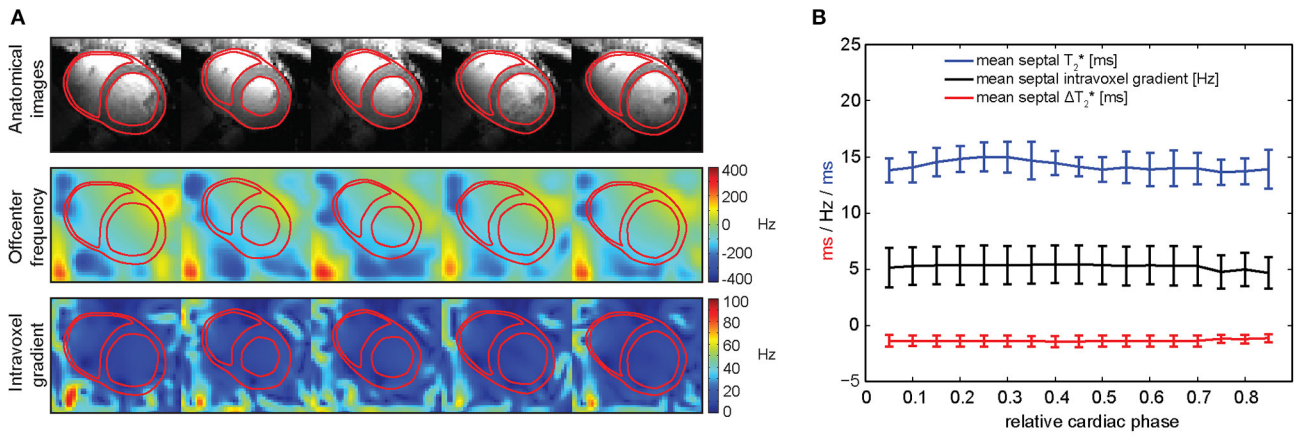

FIGURE 9 | Spatial and temporal variation of macroscopic intra-voxel B_0 gradients in the *in vivo* human heart. **(A)** Magnitude images of a short-axis view (top), in-plane macroscopic B_0 maps (middle) and intra-voxel macroscopic B_0 gradient maps (bottom) over the cardiac cycle. **(B)** Mean septal T_2^* (blue), intra-voxel B_0 gradient (black) and estimated ΔT_2^* caused by this B_0 gradient (red) over the cardiac cycle, averaged among a group of healthy volunteers. Temporal macroscopic magnetic field changes over the cardiac cycle are minor regarding their effects on T_2^* (from Huelnhagen et al. [84] with permission from John Wiley and Sons).

may lead to wrong results and eventually wrong conclusions. Second, tailored fitting procedures offer the freedom to select the most appropriate fit model, optimization approach, truncation threshold, etc. for the particular research question. Depending on the kind of application, it may for example make sense to use a bi-exponential or multi-exponential model instead of a mono-exponential approach.

In contrast to qualitative signal intensity images, relaxation maps like T_2* maps offer the advantage of providing quantitative, comparable results. Yet, effects like B_0 inhomogeneities or signal noise can impair the assessment of T_2* and lead to wrong results. Dedicated B_0 shimming approaches help to mitigate the impact of macroscopic magnetic field inhomogeneities. A reduction in voxel size can further reduce the influence of B_0 gradients on T_2* (**Figure 5B**). Yet, reducing voxel size results in an SNR loss, which can induce poor fit quality offsetting the benefit of the smaller voxel size. While a reduction in SNR might be counteracted by signal averaging and increasing acquisition times in static acquisition situations (e.g., MRI of the brain), it is often not feasible in cardiac applications, where acquisitions need to be synchronized with the cardiac cycle and where it is common to utilize breath held

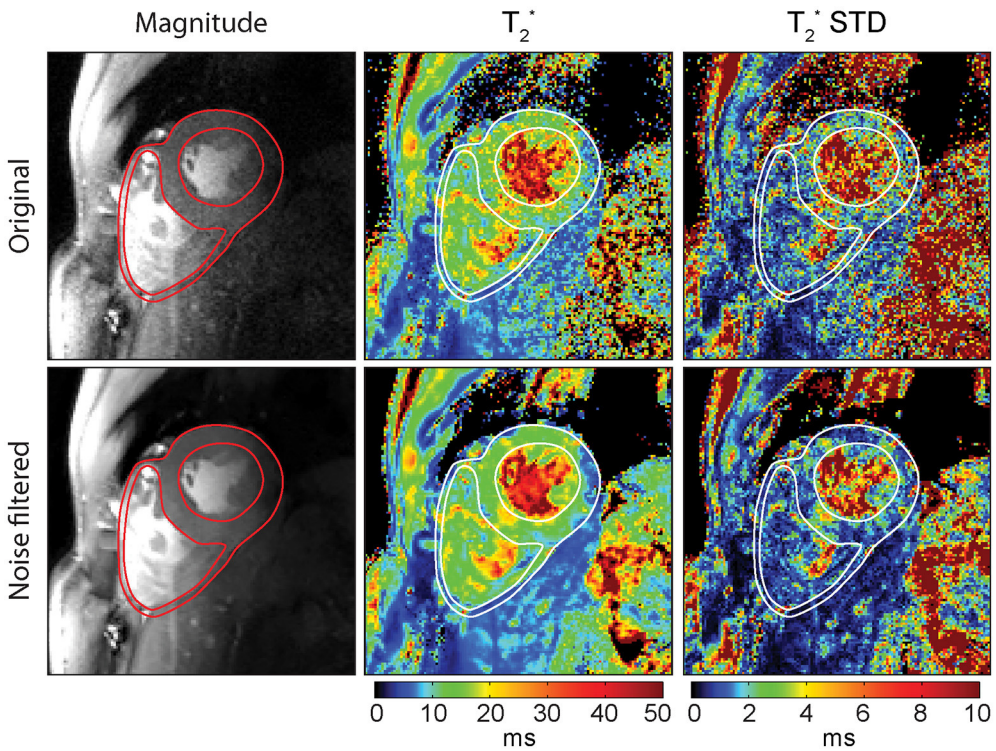

FIGURE 10 | Impact of spatially adaptive non-local means (SANLM) noise filtering on T_2^* maps of a mid-ventricular short axis view of the heart. Left: Original and SANLM filtered signal magnitude images of the first echo (TE = 2.04 ms) of a series of multi-echo gradient echo images. Center: Corresponding T_2^* maps. Right: T_2^* standard deviation maps illustrating the precision of the T_2^* maps. By applying the noise filter, an average decrease in T_2^* fit standard deviation of about 30% in the left ventricular myocardium was achieved.

conditions constraining the viable window of data acquisition to few seconds. This issue is even further pronounced in patients suffering from cardiac diseases and for acquisitions at high spatial or temporal resolution such as CINE T_2* mapping.

Image de-noising presents a viable solution to address this constraint and allows the use of small voxel sizes while still achieving acceptable fit quality. Powerful de-noising approaches like non-local means filtering [94] are readily available and can greatly improve SNR with minimal loss of information. De-noising of the T_2* maps is not recommended, because low fit quality of fitting noisy data can result in large T_2* errors that might even be enlarged or spread out by filtering. Also algorithms that estimate the noise level from the provided data will fail if presented with T_2* maps. Filtering of the magnitude images prior to fitting instead represents a robust way of improving fit quality and has been shown to increase T_2* fitting accuracy and precision [84, 95, 96] without the risk of introducing large errors. **Figure 10** illustrates an example of how T_2* mapping can benefit from noise filtering. Here a 30% reduction of T_2* fit standard deviation was achieved by noise filtering. For applications where SNR is limited such as myocardial T_2* mapping, image de-noising approaches provide a good solution to improve mapping results.

INSIGHTS FROM *IN VIVO* HUMAN MYOCARDIAL T_2* MAPPING AT ULTRAHIGH FIELDS

The technological and methodological developments in ultrahigh field CMR outlined above, permit for the first time the *in vivo* assessment of temporal myocardial T_2* changes across the cardiac cycle. Initial studies have applied these advances to gain first insights from using this technique in healthy volunteers and patients suffering from cardiovascular diseases to investigate their feasibility and potential [39, 84].

CINE Myocardial T_2* Mapping in Healthy Subjects

A first study systematically investigating the temporal changes of myocardial T_2* across the cardiac cycle in healthy subjects at 7.0 T was published in 2016 [84]. The authors analyzed the time course of myocardial T_2* throughout the cardiac cycle along with basic myocardial morphology, i.e., ventricular septal wall thickness and inner left ventricular radius as potential confounders of T_2*. The results demonstrated that myocardial T_2* obtained correlates linearly with the myocardial wall thickness [84], (**Figure 11**). The same study also showed that

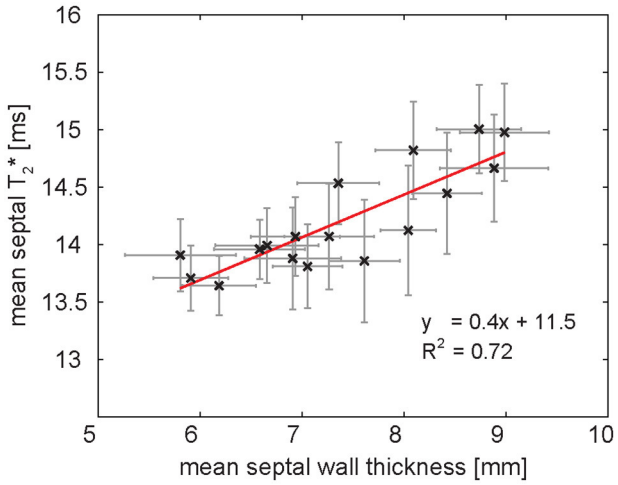

FIGURE 11 | Relationship of mean ventricular septal wall thickness and mean septal T_2^* in a group of healthy volunteers at 7.0 T. One data point corresponds to one cardiac phase. Septal wall thickness and T_2^* are linearly correlated. The result of linear regression is plotted in red. Error bars indicate SEM.

T_2* in the ventricular septum changes periodically across the cardiac cycle [84]. It increases in systole—the part of the cardiac cycle when the ventricles contract—and decreases in diastole—the part of the cardiac cycle when the heart relaxes and refills with blood (**Figure 12A**). The mean systole to diastole T_2* ratio was found to be approximately 1.1. Despite the numerous factors affecting T_2* such as blood volume fraction, hematocrit etc., myocardial T_2* is still often regarded as surrogate for tissue oxygenation. Interpreting T_2* to reflect tissue oxygenation, the observed systolic T_2* increase would imply an increase in left myocardial oxygenation during systole. This is contrary to physiological knowledge. Instead, changes in myocardial blood volume fraction induced by variations in blood pressure and resulting myocardial wall stress are believed to be responsible for the observed cyclic T_2* changes [84]. The contraction of the heart muscle compresses the intramyocardial vasculature such that inflow of arterial blood is interrupted while deoxygenated blood is squeezed out of the myocardium toward the venous coronary sinus [97–100] (**Figure 12B**). The major systolic decrease in blood volume fraction in the myocardium reduces the amount of deoxygenated hemoglobin per tissue volume, thereby increasing—instead of lowering—T_2* during systole. Previous studies of skeletal muscle have also linked T_2* changes to alterations in tissue pH and resulting changes of the tissue water content and distribution after exercise [101, 102]. These studies have examined baseline and post-exercise conditions, which are difficult to compare with the heart which is constantly exercising. Still, T_2 changes driven by tissue water content and distribution changes should be considered as a potential source of T_2* changes also in the heart. The hypothesis, that the observed periodic T_2* changes could be induced by macroscopic B_0 field variations induced by changes in bulk morphology between systole and diastole, was carefully investigated but not confirmed. Both, *in silico* magneto static simulations and *in vivo* temporally resolved B_0 mapping, showed negligible impact of cardiac morphology on the macroscopic B_0 field in the ventricular septum and hence T_2* [84].

Myocardial T_2* Mapping in Patients with Cardiovascular Diseases

Besides the application of myocardial T_2* mapping at ultrahigh magnetic fields in healthy volunteers, first investigations were carried out to explore the potential of the technique to distinguish between healthy and pathologic myocardium. These early UHF-CMR studies focused on T_2* mapping in patients with hypertrophic cardiomyopathy (HCM). HCM is the most common inherited cardiac disease affecting about 0.2–0.5% of the general population [103, 104]. The disease is characterized by an increase in myocardial wall thickness related to myocyte hypertrophy, microstructural changes like myocardial disarray, fibrosis and microvascular dysfunction. HCM patients often remain asymptomatic, but the disease can have a severe outcome in a subgroup of patients where it may cause heart failure and sudden unexpected cardiac death (SCD) in any age group. SCD and has been reported to affect about 6% of HCM patients within a mean follow up time of (8 ± 7) years [105]. This renders risk stratification vital for HCM patients. CMR plays an important role in the diagnosis and prognosis of HCM [106]. While a number of SCD risk factors in HCM have been identified such as degree of hypertrophy or presence of fibrosis the task remains challenging [107]. Consequently, basic research efforts and clinical science activities are required to better characterize HCM patient populations and to direct appropriate therapies to those at risk.

Based on the structural and physiologic changes, differences in myocardial T_2* were hypothesized in HCM patients compared to healthy controls. This hypothesis was investigated using high spatiotemporal resolution T_2* mapping at 7.0 T (**Figure 13**). It was found that septal T_2* is significantly increased in HCM with mean septal T_2* being (17.5 ± 1.4) ms in a cohort of HCM patients compared to (13.7 ± 1.1) ms in a group of gender, age and body mass index matched healthy controls. While variations of myocardial T_2* across the cardiac cycle have been attributed to changes in myocardial blood volume fraction rather than changes in tissue oxygenation [84], two main factors are assumed to cause the observed overall T_2* increase in HCM. Improved tissue oxygenation in the diseased myocardium in the case of HCM is unlikely. Instead, T_2 has been reported to be elevated in HCM [108] related to presence of inflammation and edema. A T_2 increase would also result in increased T_2* as seen from Equation (1). Further to this, reduced myocardial perfusion and ischemia are common in HCM [109], effectively reducing the tissue blood volume fraction resulting in a T_2* increase as suggested by Equation (5). These conditions are also associated with a higher risk for a poor outcome in HCM patients [110]. With this in mind it is fair to conclude that myocardial T_2* mapping could be beneficial for a better understanding of cardiac (patho)physiology *in vivo* with the ultimate goal to support risk stratification in HCM.

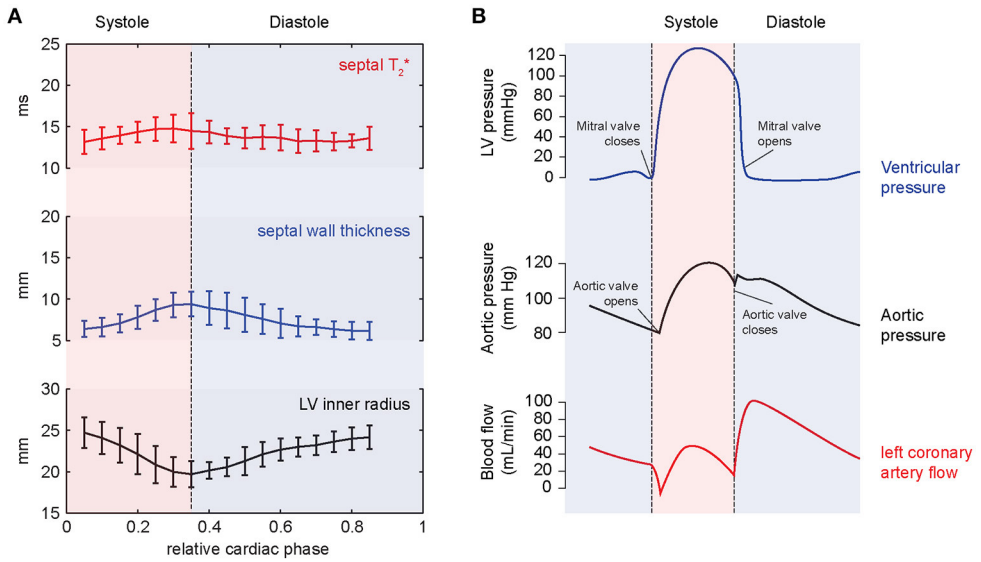

FIGURE 12 | Results of temporally resolved myocardial T_2^* mapping in healthy volunteers at 7.0 T. **(A)** Course of mean septal T_2^*, wall thickness and LV inner radius plotted over the cardiac cycle averaged for a group of healthy volunteers. Error bars indicate SD. Myocardial T_2^* changes periodically across the cardiac cycle increasing in systole and decreasing in diastole. **(B)** The periodic T_2^* changes can be explained by cyclic variations of myocardial blood volume fraction related to differences in blood pressure and myocardial wall stress. The massive pressure increase in the left ventricle in the beginning of systole results in high myocardial wall stress compressing the myocardial vessels leading to a reduced blood supply to the myocardium while blood contained in the tissue is squeezed out. The resulting reduced myocardial blood volume fraction explains the systolic T_2^* increase, which cannot be explained by increased oxygenation.

CONCLUSION AND FUTURE DIRECTIONS

The progress in myocardial T_2* mapping at ultrahigh magnetic fields is promising [111–113]. Yet, there are still a number of questions to be answered and the clinical benefit remains to be carefully investigated. This requires further efforts to tackle unsolved problems and unmet needs standing in the way *en route* to broader clinical studies. For example, the relatively long breath hold times required for the acquisition of high spatiotemporal resolution T_2* maps constitute a challenge particularly in cardiac patients. Free breathing acquisition techniques could offset this constraint permitting broader application and full 3D heart coverage. This would also help to further investigate the effect of through-plane motion. Acquisition approaches like simultaneous multi-slice excitation can be used to reduce scan times while multi-channel transmit systems can be employed to balance excitation field homogeneity and RF power deposition constraints [114, 115].

Based on the multifaceted contributions of physiological parameters on T_2* research will not stop at just mapping myocardial T_2*. Tailored acquisition schemes, data post-processing, analysis and interpretation will allow exploiting the wealth of information encoded into T_2*. For example high spatial resolution T_2* mapping facilitated by ultrahigh magnetic field strengths might be beneficial to gain a better insight into the myocardial microstructure *in vivo* with the ultimate goal to visualize myocardial fibers or to examine their helical angulation, since the susceptibility effects depend on the orientation of blood filled capillaries with regard to the external magnetic field [116]. Myocardial fiber tracking using T_2* mapping holds the promise to be less sensitive to bulk motion than diffusion-weighted MR of the myocardium [117, 118]. The increased susceptibility contrast available at 7.0 T could be exploited to quantitatively study iron accumulation in the heart with high sensitivity and spatial resolution superior to what can be achieved at 1.5 and 3.0 T. This requires the determination of norm values for healthy myocardial T_2* at 7.0 T as a mandatory precursor to broader clinical studies.

At the same time small animal studies employing cardiac disease models can provide a valuable contribution to understanding the underlying biophysical principles and (patho)physiological contrast mechanisms governing T_2*. Unlike human studies they offer the unique possibility to directly compare *in vivo* findings by MRI with *ex vivo* histology, the gold standard for tissue characterization. Recent such studies indicate that T_2* might provide not only an alternative for detection of both replacement and diffuse fibrosis without the need for exogenous contrast agents, but also has potential to distinguish the two by means of relaxation time changes induced by the presence of collagen and other fibrotic elements in the extracellular matrix [17, 18]. This could provide new diagnostic means to a large group of patients excluded from contrast agent injections due to renal insufficiencies. A study employing a mouse myocardial ischemia/reperfusion model has provided first insights into *in vivo* quantification of T_2* changes in the mouse myocardium in relation to tissue damage [16]. Local decrease of T_2* was found in the infarct

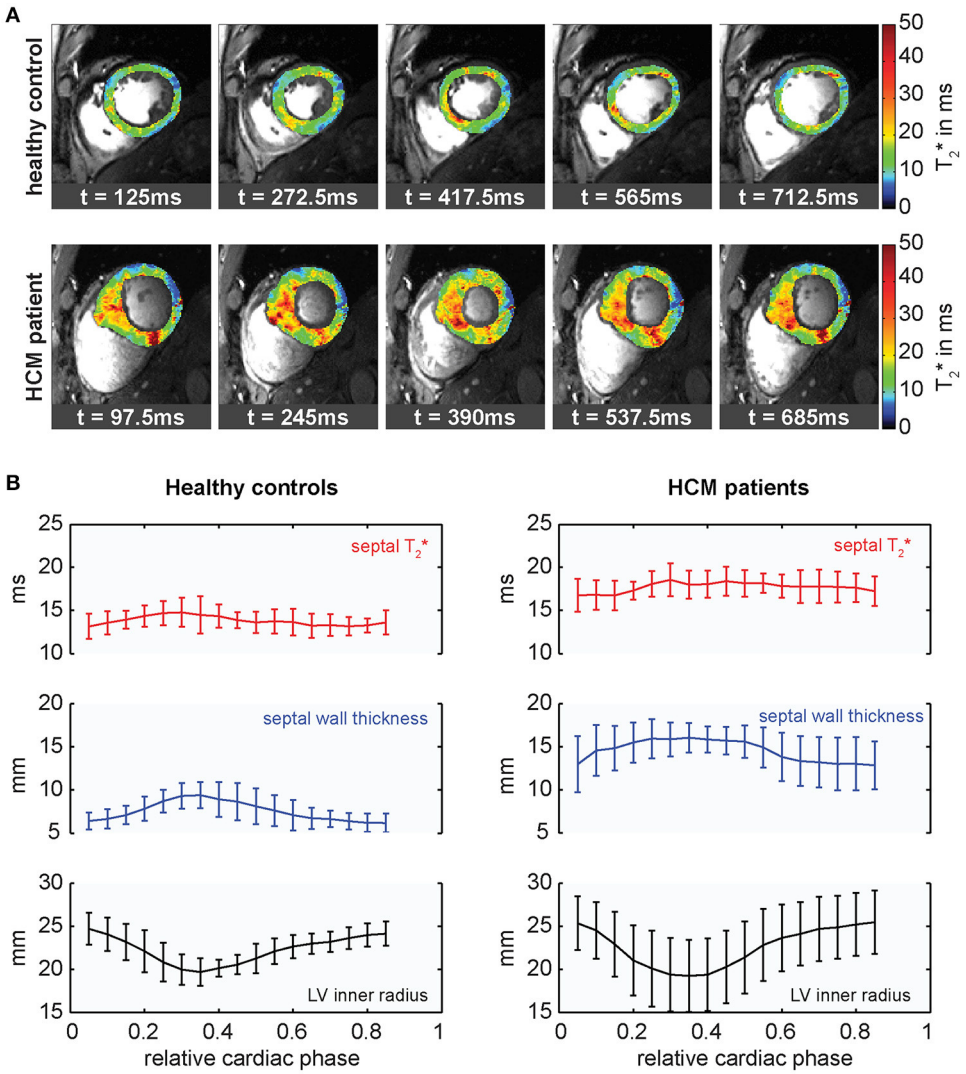

FIGURE 13 | Cardiac phase resolved myocardial T_2^* mapping in healthy volunteers and HCM patients. **(A)** Temporally resolved myocardial T_2^* maps of a short axis view of a healthy control (top) and an HCM patient (bottom), (5 out of 20 phases shown). Spatial resolution (1.1 × 1.1 × 4.0) mm^3. T_2^* variations can be observed across the cardiac cycle. **(B)** Course of mean septal T_2^*, wall thickness and inner LV radius plotted over the cardiac cycle averaged for groups of healthy controls (left) and HCM patients (right). Relative cardiac phase 0 indicates the beginning of systole. T_2^* changes periodically over the cardiac cycle increasing in systole and decreasing in diastole in both, healthy controls and HCM patients, but is significantly elevated in HCM patients.

zone and associated with deposition of collagen. The authors describe that T_2* varies dynamically during infarct development suggesting that it may be used to discriminate between acute and chronic infarctions. Taken together, by concordance the findings between human studies and cardiac disease models of small rodents will provide stronger evidence for fundamental understandings of myocyte biology, and cardiac performance with the goal to provide a more accurate diagnosis and risk stratification. Thanks to the sensitivity gain at 7.0 T the spatial fidelity feasible for T_2* mapping in humans approaches the relative anatomical spatial resolution—in terms of number of voxels with respect to anatomy—demonstrated for cardiac imaging in animal models [119, 120]. This achievement is translatable into opportunities for discovery and translational research.

The ability to probe for changes in myocardial tissue oxygenation using T_2* sensitized imaging/mapping offers the potential to address some of the spatial and temporal resolution constraints of conventional first pass perfusion imaging and holds the promise to obviate the need for exogenous contrast agents. Since microscopic susceptibility increases with field strength, thus making oxygenation sensitivity due to ischemic (patho) physiology more pronounced, T_2* mapping at 7.0 T might be beneficial to address some of the BOLD sensitivity constraints reported for the assessment of regional myocardial oxygenation changes in the presence of coronary artery

stenosis [121] or for the characterization of vasodilator-induced changes of myocardial oxygenation at 1.5 T and at 3.0 T [10].

The pace of discovery is exciting and a powerful motivator to transfer the lessons learned from T_2* mapping research at 7.0 T into the clinical scenario. These efforts are fueled by the quest for advancing the capabilities of quantitative MRI and the wish to overcome the need of exogenous contrast agent injections. The requirements of T_2* mapping at 7.0 T are likely to pave the way for further advances in MR technology and MR systems design. With appropriate multi transmit systems offering more than 16 transmit channels each providing at least 4 kW peak power, an optimistically-inclined scientist might envision the implementation of high density transceiver arrays with 64 and more elements with the ultimate goal to break ground for a many element upper torso or even a body coil array. This vision continues to motivate new research on integrated multi-channel transmission systems [122], on novel RF pulse design, on RF coil design together with explorations into ideal current patterns yielding optimal signal-to-noise-ratio for UHF-CMR [123]. Perhaps another development is the move toward myocardial T_2* mapping using reduced field of views zoomed into the target anatomy enabled by spatially selective excitation techniques which put the capabilities of parallel transmission technology to good use. With more than 45,000 examinations already performed at 7.0 T, the reasons for employing UHF-MR in translational research and for moving UHF-MR into clinical applications are more compelling than ever. This provides strong motivation to put further weight behind pushing the solution of the many remaining problems. As an important step toward this goal a system manufacturer has recently filed for FDA clearing for the clinical use of a 7.0 T system. With this development we can expect more pioneering research institutions, university hospitals and large clinics to become early adopters of CMR at 7.0 T and start harvesting knowledge and know-how that will benefit clinical applications.

ETHICS STATEMENT

In vivo studies of which data is presented in this work were carried out in accordance with the guidelines of the local ethical committee (registration number DE/CA73/5550/09, Landesamt für Arbeitsschutz, Gesundheitsschutz und technische Sicherheit, Berlin, Germany) with written informed consent from all subjects in compliance with the local institutional review board guidelines. All subjects gave written informed consent in accordance with the Declaration of Helsinki. The protocols were approved by the local ethical committee.

AUTHOR CONTRIBUTIONS

TH and TN wrote the manuscript with help from KP, MK, and TS.

FUNDING

This work was supported (in part, TH and TN) by the DZHK (German Centre for Cardiovascular Research, partner site Berlin, BER 601) and by the BMBF (Federal Ministry of Education and Research, Berlin, Germany, FKZ 81Z6100161). TN received support by the BMBF (Federal Ministry of Education and Research, Berlin, Germany, FKZ 01QE1501B) and the EUROSTARS program (E! 9340 hearRT-4-EU).

ACKNOWLEDGMENTS

The authors wish to acknowledge the team at the Berlin Ultrahigh Field Facility (B.U.F.F.) at the Max-Delbrueck Center for Molecular Medicine in the Helmholtz Association, Berlin, Germany; Jeanette Schulz-Menger from the working group for Cardiac Magnetic Resonance, Charite', Berlin, Germany; Peter Kellman (National Institutes of Health, NHLBI, Laboratory of Cardiac Energetics, Bethesda, USA); who kindly contributed examples of their pioneering work or other valuable assistance.

REFERENCES

1. von Knobelsdorff-Brenkenhoff F, Schulz-Menger J. Role of cardiovascular magnetic resonance in the guidelines of the European Society of Cardiology. *J Cardiovasc Magn Reson.* (2016) **18**:6. doi: 10.1186/s12968-016-0225-6
2. Captur G, Manisty C, Moon JC. Cardiac MRI evaluation of myocardial disease. *Heart* (2016) **102**:1429–35. doi: 10.1136/heartjnl-2015-309077
3. Ogawa S, Menon RS, Tank DW, Kim SG, Merkle H, Ellermann JM, et al. Functional brain mapping by blood oxygenation level-dependent contrast magnetic resonance imaging. A comparison of signal characteristics with a biophysical model. *Biophys J.* (1993) **64**:803–12. doi: 10.1016/S0006-3495(93)81441-3
4. Wacker CM, Hartlep AW, Pfleger S, Schad LR, Ertl G, Bauer WR. Susceptibility-sensitive magnetic resonance imaging detects human myocardium supplied by a stenotic coronary artery without a contrast agent. *J Am Coll Cardiol.* (2003) **41**:834–40. doi: 10.1016/S0735-1097(02)02931-5
5. Friedrich M, Niendorf T, Schulz-Menger J. Blood oxygen level-dependent magnetic resonance imaging in patients with stress-induced angina. *ACC Curr J Rev.* (2004) **13**:30. doi: 10.1016/j.accreview.2004.03.013
6. Jahnke C, Gebker R, Manka R, Schnackenburg B, Fleck E, Paetsch I. Navigator-gated 3D blood oxygen level–dependent CMR at 3.0-T for detection of stress-induced myocardial ischemic reactions. *JACC Cardiovasc Imaging* (2010) **3**:375–84. doi: 10.1016/j.jcmg.2009.12.008
7. Karamitsos TD, Leccisotti L, Arnold JR, Recio-Mayoral A, Bhamra-Ariza P, Howells RK, et al. Relationship between regional myocardial oxygenation and perfusion in patients with coronary artery disease insights from cardiovascular magnetic resonance and positron emission tomography. *Circ Cardiovasc Imaging* (2010) **3**:32–40. doi: 10.1161/CIRCIMAGING.109.860148
8. Tsaftaris SA, Tang R, Zhou X, Li D, Dharmakumar R. Ischemic extent as a biomarker for characterizing severity of coronary artery stenosis with blood oxygen-sensitive MRI. *J Magn Reson Imaging* (2012) **35**:1338–48. doi: 10.1002/jmri.23577
9. Wacker CM, Bock M, Hartlep AW, Beck G, van Kaick G, Ertl G, et al. Changes in myocardial oxygenation and perfusion under pharmacological

stress with dipyridamole: assessment using T*2 and T1 measurements. *Magn Reson Med.* (1999) **41**:686–95.
10. Vohringer M, Flewitt JA, Green JD, Dharmakumar R, Wang J, Jr., Tyberg JV, et al. Oxygenation-sensitive CMR for assessing vasodilator-induced changes of myocardial oxygenation. *J Cardiovasc Magn Reson.* (2010) **12**:20. doi: 10.1186/1532-429X-12-20
11. Utz W, Jordan J, Niendorf T, Stoffels M, Luft FC, Dietz R, et al. Blood oxygen level-dependent MRI of tissue oxygenation: relation to endothelium-dependent and endothelium-independent blood flow changes. *Arterioscler Thromb Vasc Biol.* (2005) **25**:1408–13. doi: 10.1161/01.ATV.0000170131.13683.d7
12. Guensch DP, Fischer K, Flewitt JA, Friedrich MG. Impact of intermittent apnea on myocardial tissue oxygenation–a study using oxygenation-sensitive cardiovascular magnetic resonance. *PLoS ONE* (2013) **8**:e53282. doi: 10.1371/journal.pone.0053282
13. Guensch DP, Fischer K, Flewitt JA, Friedrich MG. Myocardial oxygenation is maintained during hypoxia when combined with apnea–a cardiovascular MR study. *Physiol. Rep.* (2013) **1**:e00098. doi: 10.1002/phy2.98
14. Guensch DP, Fischer K, Flewitt JA, Yu J, Lukic R, Friedrich JA, et al. Breathing manoeuvre-dependent changes in myocardial oxygenation in healthy humans. *Eur Heart J Cardiovasc Imaging* (2014) **15**:409–14. doi: 10.1093/ehjci/jet171
15. Fischer K, Guensch DP, Shie N, Lebel J, Friedrich MG. Breathing maneuvers as a vasoactive stimulus for detecting inducible myocardial ischemia - an experimental cardiovascular magnetic resonance study. *PLoS ONE* (2016) **11**:e0164524. doi: 10.1371/journal.pone.0164524
16. Aguor EN, Arslan F, van de Kolk CW, Nederhoff MG, Doevendans PA, van Echteld CJ, et al. Quantitative T2* assessment of acute and chronic myocardial ischemia/reperfusion injury in mice. *Magn Reson Mater Phys Biol Med.* (2012) **25**:369–79. doi: 10.1007/s10334-012-0304-0
17. de Jong S, Zwanenburg JJ, Visser F, van der Nagel R, van Rijen HV, Vos MA, et al. Direct detection of myocardial fibrosis by MRI. *J Mol Cell Cardiol.* (2011) **51**:974–9. doi: 10.1016/j.yjmcc.2011.08.024
18. van Nierop BJ, Bax NA, Nelissen JL, Arslan F, Motaal AG, de Graaf L, et al. Assessment of myocardial fibrosis in mice using a T2*-weighted 3D radial magnetic resonance imaging sequence. *PLoS ONE* (2015) **10**:e0129899. doi: 10.1371/journal.pone.0129899
19. He T. Cardiovascular magnetic resonance T2* for tissue iron assessment in the heart. *Quant Imaging Med Surg.* (2014) **4**:407–12. doi: 10.3978/j.issn.2223-4292.2014.10.05
20. Anderson L, Holden S, Davis B, Prescott E, Charrier C, Bunce N, et al. Cardiovascular T 2-star(T 2*) magnetic resonance for the early diagnosis of myocardial iron overload. *Eur Heart J.* (2001) **22**:2171–9. doi: 10.1053/euhj.2001.2822
21. Mavrogeni S. Evaluation of myocardial iron overload using magnetic resonance imaging. *Blood Transfusion* (2009) **7**:183–7. doi: 10.2450/2008.0063-08
22. Carpenter J-P, He T, Kirk P, Roughton M, Anderson LJ, de Noronha SV, et al. On T2* magnetic resonance and cardiac iron. *Circulation* (2011) **123**:1519–28. doi: 10.1161/CIRCULATIONAHA.110.007641
23. Friedrich MG, Karamitsos TD. Oxygenation-sensitive cardiovascular magnetic resonance. *J Cardiovasc Magn Reson.* (2013) **15**:43. doi: 10.1186/1532-429X-15-43
24. Haacke EM, Brown RW, Thompson MR, Venkatesan R, editors. Magnetization, relaxation and the bloch equation. In: *Magnetic Resonance Imaging - Physical Principles and Sequence Design*. 1st ed. New York, NY: John Wiley & Sons (1999). p. 51–64.
25. Zhao JM, Clingman CS, Närväinen MJ, Kauppinen RA, van Zijl P. Oxygenation and hematocrit dependence of transverse relaxation rates of blood at 3T. *Magn. Reson. Med.* (2007) **58**:592–7. doi: 10.1002/mrm.21342
26. Ogawa S, Lee TM, Kay AR, Tank DW. Brain magnetic resonance imaging with contrast dependent on blood oxygenation. *Proc Natl Acad Sci USA.* (1990) **87**:9868–72. doi: 10.1073/pnas.87.24.9868
27. Brown RW, Cheng Y-CN, Haacke EM, Thompson MR, Venkatesan R. *Magnetic Resonance Imaging*: *Physical Principles and Sequence Design*. New York, NY: John Wiley & Sons (2014).
28. Bernstein MA, King KF, Zhou XJ. *Handbook of MRI Pulse Sequences*. New York, NY: Elsevier (2004).
29. Ogawa S, Tank DW, Menon R, Ellermann JM, Kim SG, Merkle H, et al. Intrinsic signal changes accompanying sensory stimulation: functional brain mapping with magnetic resonance imaging. *Proc Natl Acad Sci USA.* (1992) **89**:5951–5. doi: 10.1073/pnas.89.13.5951
30. Bauer WR, Nadler W, Bock M, Schad LR, Wacker C, Hartlep A, et al. Theory of the BOLD effect in the capillary region: an analytical approach for the determination of T2 in the capillary network of myocardium. *Magn Reson Med.* (1999) **41**:51–62.
31. Guensch DP, Nadeshalingam G, Fischer K, Stalder AF, Friedrich MG. The impact of hematocrit on oxygenation-sensitive cardiovascular magnetic resonance. *J Cardiovasc Magn Reson.* (2016) **18**:42. doi: 10.1186/s12968-016-0262-1
32. Yablonskiy DA, Haacke EM. Theory of NMR signal behavior in magnetically inhomogeneous tissues: the static dephasing regime. *Magn Reson Med.* (1994) **32**:749–63. doi: 10.1002/mrm.1910320610
33. Christen T, Lemasson B, Pannetier N, Farion R, Segebarth C, Rémy C, et al. Evaluation of a quantitative blood oxygenation level-dependent (qBOLD) approach to map local blood oxygen saturation. *NMR Biomed.* (2011) **24**:393–403. doi: 10.1002/nbm.1603
34. Spees WM, Yablonskiy DA, Oswood MC, Ackerman JJ. Water proton MR properties of human blood at 1.5 tesla: magnetic susceptibility, T1, T2, T2*, and non-lorentzian signal behavior. *Magn Reson Med.* (2001) **45**:533–42. doi: 10.1002/mrm.1072
35. Niendorf T, Pohlmann A, Arakelyan K, Flemming B, Cantow K, Hentschel J, et al. How bold is blood oxygenation level-dependent (BOLD) magnetic resonance imaging of the kidney? Opportunities, challenges and future directions. *Acta Physiol.* (2015) **213**:19–38. doi: 10.1111/apha.12393
36. Meloni A, Hezel F, Positano V, Keilberg P, Pepe A, Lombardi M, et al. Detailing magnetic field strength dependence and segmental artifact distribution of myocardial effective transverse relaxation rate at 1.5, 3.0, and 7.0 T. *Magn Reson Med.* (2014) **71**:2224–30. doi: 10.1002/mrm.24856
37. Ocali O, Atalar E. Ultimate intrinsic signal-to-noise ratio in MRI. *Magn Reson Med.* (1998) **39**:462–73. doi: 10.1002/mrm.1910390317
38. Ugurbil K, Adriany G, Andersen P, Chen W, Garwood M, Gruetter R, et al. Ultrahigh field magnetic resonance imaging and spectroscopy. *Magn Reson Imaging* (2003) **21**:1263–81. doi: 10.1016/j.mri.2003.08.027
39. Hezel F, Thalhammer C, Waiczies S, Schulz-Menger J, Niendorf T. High spatial resolution and temporally resolved T_2^* mapping of normal human myocardium at 7.0 tesla: an ultrahigh field magnetic resonance feasibility study. *PLoS ONE* (2012) **7**:e52324. doi: 10.1371/journal.pone.0052324
40. Mueller A, Kouwenhoven M, Naehle CP, Gieseke J, Strach K, Willinek WA, et al. Dual-source radiofrequency transmission with patient-adaptive local radiofrequency shimming for 3.0-T cardiac mr imaging: initial experience. *Radiology* (2012) **263**:77–85. doi: 10.1148/radiol.11110347
41. Vaughan JT, Snyder CJ, DelaBarre LJ, Bolan PJ, Tian J, Bolinger L, et al. Whole-body imaging at 7T: preliminary results. *Magn Reson Med.* (2009) **61**:244–8. doi: 10.1002/mrm.21751
42. Snyder CJ, DelaBarre L, Metzger GJ, van de Moortele PF, Akgun C, Ugurbil K, et al. Initial results of cardiac imaging at 7 Tesla. *Magn Reson Med.* (2009) **61**:517–24. doi: 10.1002/mrm.21895
43. Maderwald S, Orzada S, Schaefer LC, Bitz AK, Brote I, Kraff O, et al., editors. 7T Human *in vivo* cardiac imaging with an 8-channel transmit/receive array. In: *Proceedings of the International Society for Magnetic Resonance Medicine.* Honolulu, HI (2009).
44. van den Bergen B, Klomp DW, Raaijmakers AJ, de Castro CA, Boer VO, Kroeze H, et al. Uniform prostate imaging and spectroscopy at 7 T: comparison between a microstrip array and an endorectal coil. *NMR Biomed.* (2011) **24**:358–65. doi: 10.1002/nbm.1599
45. Ipek O, Raaijmakers AJ, Klomp DW, Lagendijk JJ, Luijten PR, van den Berg CA. Characterization of transceive surface element designs for 7 tesla magnetic resonance imaging of the prostate: radiative antenna and microstrip. *Phys Med Biol.* (2012) **57**:343–55. doi: 10.1088/0031-9155/57/2/343

46. Winter L, Özerdem C, Hoffmann W, Santoro D, Müller A, Waiczies H, et al. Design and evaluation of a hybrid radiofrequency applicator for magnetic resonance imaging and RF induced hyperthermia: electromagnetic field simulations up to 14.0 tesla and proof-of-concept at 7.0 tesla. *PLoS ONE* (2013) **8**:e61661. doi: 10.1371/journal.pone.0061661
47. Oezerdem C, Winter L, Graessl A, Paul K, Els A, Weinberger O, et al. 16-channel bow tie antenna transceiver array for cardiac MR at 7.0 tesla. *Magn Reson Med.* (2016) **75**:2553–65. doi: 10.1002/mrm.25840
48. Raaijmakers AJ, Ipek O, Klomp DW, Possanzini C, Harvey PR, Lagendijk JJ, et al. Design of a radiative surface coil array element at 7 T: the single-side adapted dipole antenna. *Magn Reson Med.* (2011) **66**:1488–97. doi: 10.1002/mrm.22886
49. Ipek O, Raaijmakers AJ, Lagendijk JJ, Luijten PR, van den Berg CA. Intersubject local SAR variation for 7T prostate MR imaging with an eight-channel single-side adapted dipole antenna array. *Magn Reson Med.* (2014) **71**:1559–67. doi: 10.1002/mrm.24794
50. Erturk MA, Raaijmakers AJ, Adriany G, Ugurbil K, Metzger GJ. A 16-channel combined loop-dipole transceiver array for 7 Tesla body MRI. *Magn Reson Med.* (2017) **77**:884–94. doi: 10.1002/mrm.26153
51. Raaijmakers AJE, Italiaander M, Voogt IJ, Luijten PR, Hoogduin JM, Klomp DWJ, et al. The fractionated dipole antenna: a new antenna for body imaging at 7 Tesla. *Magn Reson Med.* (2016) **75**:1366–74. doi: 10.1002/mrm.25596
52. Aussenhofer SA, Webb AG. An eight-channel transmit/receive array of TE_{01} mode high permittivity ceramic resonators for human imaging at 7T. *J Magn Reson.* (2014) **243**:122–9. doi: 10.1016/j.jmr.2014.04.001
53. Alon L, Deniz CM, Brown R, Sodickson DK, Collins CM, editors. A slot antenna concept for high fidelity body imaging at ultra high field. In: *Proceedings of the International Society for Magnetic Resonance Medicine.* Singapore (2016).
54. Versluis MJ, Tsekos N, Smith NB, Webb AG. Simple RF design for human functional and morphological cardiac imaging at 7tesla. *J Magn Reson.* (2009) **200**:161–6. doi: 10.1016/j.jmr.2009.06.014
55. Dieringer MA, Renz W, Lindel T, Seifert F, Frauenrath T, von Knobelsdorff-Brenkenhoff F, et al. Design and application of a four-channel transmit/receive surface coil for functional cardiac imaging at 7T. *J Magn Reson Imaging* (2011) **33**:736–41. doi: 10.1002/jmri.22451
56. Thalhammer C, Renz W, Winter L, Hezel F, Rieger J, Pfeiffer H, et al. Two-Dimensional sixteen channel transmit/receive coil array for cardiac MRI at 7.0 T: design, evaluation, and application. *J Magn Reson Imaging* (2012) **36**:847–57. doi: 10.1002/jmri.23724
57. Winter L, Kellman P, Renz W, Gräßl A, Hezel F, Thalhammer C, et al. Comparison of three multichannel transmit/receive radiofrequency coil configurations for anatomic and functional cardiac MRI at 7.0T: implications for clinical imaging. *Eur Radiol.* (2012) **22**:2211–20. doi: 10.1007/s00330-012-2487-1
58. Graessl A, Winter L, Thalhammer C, Renz W, Kellman P, Martin C, et al. Design, evaluation and application of an eight channel transmit/receive coil array for cardiac MRI at 7.0 T. *Eur J. Radiol.* (2013) **82**:752–9. doi: 10.1016/j.ejrad.2011.08.002
59. Graessl A, Renz W, Hezel F, Dieringer MA, Winter L, Oezerdem C, et al. Modular 32-channel transceiver coil array for cardiac MRI at 7.0T. *Magn Reson Med.* (2014) **72**:276–90. doi: 10.1002/mrm.24903
60. Adriany G, Ritter J, Vaughan JT, Ugurbil K, Moortele PF, editors. Experimental verification of enhanced B1 shim performance with a Z-encoding RF coil array at 7 Tesla. In: *Proceedings of the International Society for Magnetic Resonance Medicine.* Stockholm (2010).
61. Frauenrath T, Hezel F, Renz W, de Geyer TdO, Dieringer M, Knobelsdorff-Brenkenhoff FV, et al. Acoustic cardiac triggering: a practical solution for synchronization and gating of cardiovascular magnetic resonance at 7 Tesla. *J Cardiovasc Magn Reson.* (2010) **12**:67. doi: 10.1186/1532-429X-12-67
62. Togawa T, Okai O, Oshima M. Observation of blood flow E.M.F. in externally applied strong magnetic field by surface electrodes. *Med Biol Eng.* (1967) **5**:169–70. doi: 10.1007/BF02474505
63. Stuber M, Botnar RM, Fischer SE, Lamerichs R, Smink J, Harvey P, et al. Preliminary report on *in vivo* coronary MRA at 3 Tesla in humans. *Magn Reson Med.* (2002) **48**:425–9. doi: 10.1002/mrm.10240
64. Lanzer P, Barta C, Botvinick EH, Wiesendanger HU, Modin G, Higgins CB. ECG-synchronized cardiac MR imaging: method and evaluation. *Radiology* (1985) **155**:681–6. doi: 10.1148/radiology.155.3.4001369
65. Fischer SE, Wickline SA, Lorenz CH. Novel real-time R-wave detection algorithm based on the vectorcardiogram for accurate gated magnetic resonance acquisitions. *Magn Reson Med.* (1999) **42**:361–70.
66. Chia JM, Fischer SE, Wickline SA, Lorenz CH. Performance of QRS detection for cardiac magnetic resonance imaging with a novel vectorcardiographic triggering method. *J Magn Reson Imaging* (2000) **12**:678–88. doi: 10.1002/1522-2586(200011)12:5<678::aid-jmri4>3.0.co;2-5
67. Becker M, Frauenrath T, Hezel F, Krombach GA, Kremer U, Koppers B, et al. Comparison of left ventricular function assessment using phonocardiogram- and electrocardiogram-triggered 2D SSFP CINE MR imaging at 1.5 T and 3.0 T. *Eur Radiol.* (2010) **20**:1344–55. doi: 10.1007/s00330-009-1676-z
68. Frauenrath T, Hezel F, Heinrichs U, Kozerke S, Utting JF, Kob M, et al. Feasibility of cardiac gating free of interference with electro-magnetic fields at 1.5 Tesla, 3.0 Tesla and 7.0 Tesla using an MR-stethoscope. *Invest Radiol.* (2009) **44**:539–47. doi: 10.1097/RLI.0b013e3181b4c15e
69. Brandts A, Westenberg JJ, Versluis MJ, Kroft LJ, Smith NB, Webb AG, et al. Quantitative assessment of left ventricular function in humans at 7 T. *Magn Reson Med.* (2010) **64**:1471–7. doi: 10.1002/mrm.22529
70. Frauenrath T, Niendorf T, Malte K. Acoustic method for synchronization of magnetic resonance imaging (MRI). *Acta Acust. United Acust.* (2008) **94**:148–55. doi: 10.3813/AAA.918017
71. Krug JW, Rose G, Clifford GD, Oster J. ECG-based gating in ultra high field cardiovascular magnetic resonance using an independent component analysis approach. *J Cardiovasc Magn Reson.* (2013) **15**:104. doi: 10.1186/1532-429X-15-104
72. Gregory TS, Schmidt EJ, Zhang SH, Ho Tse ZT. 3DQRS: a method to obtain reliable QRS complex detection within high field MRI using 12-lead electrocardiogram traces. *Magn Reson Med.* (2014) **71**:1374–80. doi: 10.1002/mrm.25078
73. Kosch O, Thiel F, Di Clemente FS, Hein M, Seifert F, editors. Monitoring of human cardio-pulmonary activity by multi-channel UWB-radar. *Antennas and Propagation in Wireless Communications (APWC), 2011 IEEE-APS Topical Conference on.* Torino: IEEE (2011).
74. Gross S, Vionnet L, Kasper L, Dietrich BE, Pruessmann KP. Physiology recording with magnetic field probes for fMRI denoising. *Neuroimage* (in press). doi: 10.1016/j.neuroimage.2017.01.022. [Epub ahead of print].
75. Maclaren J, Aksoy M, Bammer R. Contact-free physiological monitoring using a markerless optical system. *Magn Reson Med.* (2015) **74**:571–7. doi: 10.1002/mrm.25781
76. Fuchs K, Hezel F, Winter L, Oezerdem C, Graessl A, Dieringer M, et al., editors. Feasibility of cardiac fast spin echo imaging at 7.0 T using a two-dimensional 16 channel array of bowtie transceivers. In: *Proceedings of the International Society for Magnetic Resonance Medicine.* Salt Lake City (2013).
77. Norris DG, Boernert P, Reese T, Leibfritz D. On the application of ultra-fast rare experiments. *Magn Reson Med.* (1992) **27**:142–64. doi: 10.1002/mrm.1910270114
78. Carr HY, Purcell EM. Effects of diffusion on free precession in nuclear magnetic resonance experiments. *Phys Rev.* (1954) **94**:630–8. doi: 10.1103/PhysRev.94.630
79. Meiboom S, Gill D. Modified spin-echo method for measuring nuclear relaxation times. *Rev Sci Instrum.* (1958) **29**:688–91. doi: 10.1063/1.1716296
80. Heinrichs U, Utting JF, Frauenrath T, Hezel F, Krombach GA, Hodenius MA, et al. Myocardial T2* mapping free of distortion using susceptibility-weighted fast spin-echo imaging: a feasibility study at 1.5 T and 3.0 T. *Magn Reson Med.* (2009) **62**:822–8. doi: 10.1002/mrm.22054
81. Schick F. SPLICE: sub-second diffusion-sensitive MR imaging using a modified fast spin-echo acquisition mode. *Magn Reson Med.* (1997) **38**:638–44. doi: 10.1002/mrm.1910380418
82. Haacke E, Brown R, Thompson M, Venkatesan R, Bernstein M, King K, et al. *Magnetic Resonance Imaging - Physical Principles and Sequence Design*. New York, NY: John Wiley and Sons (1999).

83. Robinson S, Schodl H, Trattnig S. A method for unwrapping highly wrapped multi-echo phase images at very high field: UMPIRE. *Magn Reson Med.* (2013) **72**:80–92. doi: 10.1002/mrm.24897
84. Huelnhagen T, Hezel F, Serradas Duarte T, Pohlmann A, Oezerdem C, Flemming B, et al. Myocardial effective transverse relaxation time T2* correlates with left ventricular wall thickness: a 7.0 T MRI study. *Magn Reson Med.* (2016) **77**:2381–9. doi: 10.1002/mrm.26312
85. Jaffer FA, Wen H, Balaban RS, Wolff SD. A method to improve the BO homogeneity of the heart *in vivo*. *Magn Reson Med.* (1996) **36**:375–83. doi: 10.1002/mrm.1910360308
86. Schar M, Kozerke S, Fischer SE, Boesiger P. Cardiac SSFP imaging at 3 Tesla. *Magn Reson Med.* (2004) **51**:799–806. doi: 10.1002/mrm.20024
87. Schar M, Vonken EJ, Stuber M. Simultaneous B(0)- and B(1)+-map acquisition for fast localized shim, frequency, and RF power determination in the heart at 3 T. *Magn Reson Med.* (2010) **63**:419–26. doi: 10.1002/mrm.22234
88. Reeder SB, Faranesh AZ, Boxermann JL, McVeigh ER. *In vivo* measurement of T_2^* and field inhomogeneity maps in the human heart at 1.5 T. *Magn Reson Med.* (1998) **39**:988–98. doi: 10.1002/mrm.1910390617
89. Shah S, Kellman P, Greiser A, Weale PJ, Zuehlsdorff S, Jerecic R, editors. Rapid fieldmap estimation for cardiac shimming. In: *Proceedings of the International Society for Magnetic Resonance Medicine 17*. Honolulu, HI (2009).
90. Serradas Duarte T, Huelnhagen T, Niendorf T, editors. Assessment of myocardial B0 over the cardiac cycle at 7.0T: implications for susceptibility-based cardiac MR techniques. In: *Proceedings of the International Society for Magnetic Resonance Medicine 24*. Singapore (2016).
91. Serradas Duarte T. *Detailing Myocardial B0 across the Cardiac Cycle at UHF: B0 Assessment and Implications for Susceptibility-based CMR Techniques*. Lisbon: Universidade Nova de Lisboa (2016).
92. Kelley CT. *Iterative Methods for Optimization*. Philadelphia: Siam (1999).
93. Sandino CM, Kellman P, Arai AE, Hansen MS, Xue H. Myocardial T2* mapping: influence of noise on accuracy and precision. *J Cardiovasc Magn Reson.* (2015) **17**:7. doi: 10.1186/s12968-015-0115-3
94. Manjon JV, Coupe P, Marti-Bonmati L, Collins DL, Robles M. Adaptive non-local means denoising of MR images with spatially varying noise levels. *J Magn Reson Imaging* (2010) **31**:192–203. doi: 10.1002/jmri.22003
95. Feng Y, He T, Feng M, Carpenter JP, Greiser A, Xin X, et al. Improved pixel-by-pixel MRI R2* relaxometry by nonlocal means. *Magn Reson Med.* (2014) **72**:260–8. doi: 10.1002/mrm.24914
96. Huelnhagen T, Pohlmann A, Niendorf T, editors. Improving T2* mapping accuracy by spatially adaptive non-local means noise filtering. In: *Proceedings of the International Society for Magnetic Resonance Medicine 23*. Toronto, ON (2015).
97. Guyton AC, Hall JE, editors. Muscle blood flow and cardiac output during exercise; the coronary circulation and ischemic heart disease. In: *Guyton and Hall Textbook of Medical Physiology*. 10th ed. Philadelphia: Saunders (2000). p. 223–34.
98. Schmidt RF, Lang F, Heckmann M. Herzmechanik. *Physiologie des Menschen: Mit Pathophysiologie*. 31st ed. Heidelberg: Springer (2010). p. 539–64.
99. Deussen A. Herzstoffwechsel und Kroronardurchblutung. In: Schmidt RF, Lang F, Heckmann M, editors. *Physiologie des Menschen: Mit Pathophysiologie*. 31st ed. Heidelberg: Springer (2010). p. 565–71.
100. Judd RM, Levy BI. Effects of barium-induced cardiac contraction on large- and small-vessel intramyocardial blood volume. *Circ Res.* (1991) **68**:217–25. doi: 10.1161/01.RES.68.1.217
101. Fleckenstein JL, Canby RC, Parkey RW, Peshock RM. Acute effects of exercise on MR imaging of skeletal muscle in normal volunteers. *AJR Am J Roentgenol.* (1988) **151**:231–7. doi: 10.2214/ajr.151.2.231
102. Schmid AI, Schewzow K, Fiedler GB, Goluch S, Laistler E, Wolzt M, et al. Exercising calf muscle T2* changes correlate with pH, PCr recovery and maximum oxidative phosphorylation. *NMR Biomed.* (2014) **27**:553–60. doi: 10.1002/nbm.3092
103. Mozaffarian D, Benjamin EJ, Go AS, Arnett DK, Blaha MJ, Cushman M, et al. Heart disease and stroke statistics—2016 update a report from the american heart association. *Circulation* (2015) **133**:e38–360. doi: 10.1161/CIR.0000000000000350
104. Kramer CM, Appelbaum E, Desai MY, Desvigne-Nickens P, DiMarco JP, Friedrich MG, et al. Hypertrophic Cardiomyopathy Registry: the rationale and design of an international, observational study of hypertrophic cardiomyopathy. *Am Heart J.* (2015) **170**:223–30. doi: 10.1016/j.ahj.2015.05.013
105. Maron BJ, Olivotto I, Spirito P, Casey SA, Bellone P, Gohman TE, et al. Epidemiology of hypertrophic cardiomyopathy–related death revisited in a large non-referral-based patient population. *Circulation* (2000) **102**:858–64. doi: 10.1161/01.CIR.102.8.858
106. Noureldin RA, Liu S, Nacif MS, Judge DP, Halushka MK, Abraham TP, et al. The diagnosis of hypertrophic cardiomyopathy by cardiovascular magnetic resonance. *J Cardiovasc Magn Reson.* (2012) **14**:17. doi: 10.1186/1532-429X-14-17
107. Steriotis AK, Sharma S. Risk stratification in hypertrophic cardiomyopathy. *Eur Cardiol Rev.* (2015) **10**:31–6. doi: 10.15420/ecr.2015.10.01.31
108. Abdel-Aty H, Cocker M, Strohm O, Filipchuk N, Friedrich MG. Abnormalities in T2-weighted cardiovascular magnetic resonance images of hypertrophic cardiomyopathy: regional distribution and relation to late gadolinium enhancement and severity of hypertrophy. *J Magn Reson Imaging* (2008) **28**:242–5. doi: 10.1002/jmri.21381
109. Johansson B, Mörner S, Waldenström A, Stål P. Myocardial capillary supply is limited in hypertrophic cardiomyopathy: a morphological analysis. *Int J Cardiol.* (2008) **126**:252–7. doi: 10.1016/j.ijcard.2007.04.003
110. Cecchi F, Olivotto I, Gistri R, Lorenzoni R, Chiriatti G, Camici PG. Coronary microvascular dysfunction and prognosis in hypertrophic cardiomyopathy. *New Engl J. Med.* (2003) **349**:1027–35. doi: 10.1056/NEJMoa025050
111. Niendorf T, Graessl A, Thalhammer C, Dieringer MA, Kraus O, Santoro D, et al. Progress and promises of human cardiac magnetic resonance at ultrahigh fields: a physics perspective. *J Magn Reson.* (2013) **229**:208–22. doi: 10.1016/j.jmr.2012.11.015
112. Niendorf T, Sodickson DK, Krombach GA, Schulz-Menger J. Toward cardiovascular MRI at 7 T: clinical needs, technical solutions and research promises. *Eur Radiol.* (2010) **20**:2806–16. doi: 10.1007/s00330-010-1902-8
113. Niendorf T, Paul K, Oezerdem C, Graessl A, Klix S, Huelnhagen T, et al. W(h)ither human cardiac and body magnetic resonance at ultrahigh fields? Technical advances, practical considerations, applications, and clinical opportunities. *NMR Biomed.* (2016) **29**:1173–97. doi: 10.1002/nbm.3268
114. Schmitter S, Wu X, Uğurbil K, de Moortele V. Design of parallel transmission radiofrequency pulses robust against respiration in cardiac MRI at 7 Tesla. *Magn Reson Med.* (2015) **74**:1291–305. doi: 10.1002/mrm.25512
115. Schmitter S, Moeller S, Wu X, Auerbach EJ, Metzger GJ, Van de Moortele PF, et al. Simultaneous multislice imaging in dynamic cardiac MRI at 7T using parallel transmission. *Magn Reson Med.* (2016) **77**:1010–20. doi: 10.1002/mrm.26180.
116. Reichenbach JR, Haacke EM. High-resolution BOLD venographic imaging: a window into brain function. *NMR Biomed.* (2001) **14**:453–67. doi: 10.1002/nbm.722
117. Reese TG, Weisskoff RM, Smith RN, Rosen BR, Dinsmore RE, Wedeen VJ. Imaging myocardial fiber architecture *in vivo* with magnetic resonance. *Magn Reson Med.* (1995) **34**:786–91. doi: 10.1002/mrm.1910340603
118. Wu MT, Tseng WY, Su MY, Liu CP, Chiou KR, Wedeen VJ, et al. Diffusion tensor magnetic resonance imaging mapping the fiber architecture remodeling in human myocardium after infarction: correlation with viability and wall motion. *Circulation* (2006) **114**:1036–45. doi: 10.1161/CIRCULATIONAHA.105.545863
119. Wagenhaus B, Pohlmann A, Dieringer MA, Els A, Waiczies H, Waiczies S, et al. Functional and morphological cardiac magnetic resonance imaging of mice using a cryogenic quadrature radiofrequency coil. *PLoS ONE* (2012) **7**:e42383. doi: 10.1371/journal.pone.0042383

120. Niendorf T, Pohlmann A, Reimann HM, Waiczies H, Peper E, Huelnhagen T, et al. Advancing cardiovascular, neurovascular, and renal magnetic resonance imaging in small rodents using cryogenic radiofrequency coil technology. *Front Pharmacol.* (2015) **6**:255. doi: 10.3389/fphar.2015.00255
121. Dharmakumar R, Arumana JM, Tang R, Harris K, Zhang Z, Li D. Assessment of regional myocardial oxygenation changes in the presence of coronary artery stenosis with balanced SSFP imaging at 3.0 T: theory and experimental evaluation in canines. *J Magn Reson Imaging* (2008) **27**:1037–45. doi: 10.1002/jmri.21345
122. Poulo L, Alon L, Deniz C, Haefner R, Sodickson D, Stoeckel B, et al. A 32-Channel parallel exciter/amplifier transmit system for 7T imaging. In: ISMRM, editor. *Proceedings of the International Society for Magnetic Resonance Medicine 19*. Montréal (2011). p. 1867.
123. Lattanzi R, Sodickson DK. Ideal current patterns yielding optimal signal-to-noise ratio and specific absorption rate in magnetic resonance imaging: computational methods and physical insights. *Magn Reson Med.* (2012) **68**:286–304. doi: 10.1002/mrm.23198

Conflict of Interest Statement: TN is founder and CEO of MRI.TOOLS GmbH, Berlin, Germany.

The reviewer AIS and handling Editor declared their shared affiliation, and the handling Editor states that the process nevertheless met the standards of a fair and objective review.

The other authors declare that the research was conducted in the absence of any commercial or financial relationships that could be construed as a potential conflict of interest.